Residual liquid from deep magma ocean crystallization in the source of komatiites from the ICDP drill core in the Barberton Greenstone Belt

Maud Boyet, Marion Garçon, N. Arndt, R.W. Carlson, Z. Konc

Residual liquid from deep magma ocean crystallization in the source of komatiites from the ICDP drill core in the Barberton Greenstone Belt

Boyet M.[1], Garçon M.[1], Arndt N.[2], Carlson R.W.[4], Konc Z.[1]

[1] Université Clermont Auvergne, CNRS, IRD, OPGC, Laboratoire Magmas et Volcans, F-63000 Clermont-Ferrand, France

[2] ISTerre, UMR 5275, CNRS, Université Grenoble-Alpes, BP 53, FR-38041 Grenoble CEDEX 09, France

[3] Carnegie Institution for Science, Earth and Planets Laboratory, 5241 Broad Branch Road, NW, Washington DC 20015-1305, United States

Manuscript length: 6968 words
Figures: 10 (+ 3 supplementary figures)
Tables: 3
References: 58

ABSTRACT

Komatiites and sedimentary rocks sampled during the International Continental Drilling Program (BARB1-2-3-4-5) in the Barberton greenstone belt, South Africa, were analyzed for ^{146}Sm-^{142}Nd systematics. Resolved negative μ^{142}Nd values (down to -7.7 ± 2.8) were identified in komatiites from the 3.48 Ga Komati Formation and this signature correlates with low Hf/Sm ratios measured in these samples. The negative μ^{142}Nd point to a source with subchondritic Sm/Nd ratio which formed during the Hadean. No analytically resolvable ^{142}Nd anomalies were measured in crustal detritus-rich, Si-rich, Ca-Fe-rich sediments and cherts from the Buck Reef (3.42 Ga) and the Fig Tree Group (3.23-3.28 Ga). Our new measurements are incorporated into a larger set of ^{147}Sm-^{143}Nd and ^{176}Lu-^{176}Hf data to better understand

the ^{142,143}Nd-^{176}Hf isotope signatures in the mantle source at the time of komatiite crystallization. Our calculations show that the ^{142,143}Nd-^{176}Hf isotope signatures and Hf/Sm ratios cannot be produced by recycling into the komatiite source of detrital sediments like those sampled in the Barberton area. Only cherts have the required trace element characteristics – low Hf/Sm, radiogenic ε^{176}Hf –but the trace element concentrations in the cherts are so low that unrealistic amounts of chert would need to be added.

We propose a four-stage model for the formation of these rocks. Negative μ^{142}Nd and low Hf/Sm ratios developed during the crystallization of a deep magma ocean soon after Earth accretion. The material that ultimately became the source of komatiites was a residual liquid produced by 50% crystallization leaving a bridgmanite/ferropericlase/Ca-perovskite cumulate. The Lu-Hf and Sm-Nd isotope systems were decoupled at this stage. After extinction of ^{146}Sm around 4 Ga, parent/daughter ratios fractionated during a melt extraction event. With this model we explain the positive ε^{176}Hf and slightly negative ε^{143}Nd in these samples. The 3.55 Ga Schapenburg komatiites in another part of the Barberton belt share similar chemical signatures, supporting our model of fractionation in a deep magma ocean early in Earth history.

1. INTRODUCTION

Short- and long-lived radiogenic isotope systems provide strong constraints on the composition, chemical differentiation and dynamics of the mantle. Studies of Archean samples provide key information on the timing and processes that drove the evolution of the early mantle and formation of the first crust (e.g. Carlson et al., 2019). Particularly important are komatiites – ultramafic volcanic rocks found mainly in Archean greenstone belts. Convincing petrological evidence indicates that these rocks were derived from the deep mantle, and they therefore yield valuable information on part of the early mantle that is rarely accessible (Ohtani, 1984; Herzberg, 1992; Arndt et al., 2008).

The 3.5-3.0 Ga Barberton greenstone belt (BGB) in South Africa, together with the Pilbara in Australia, contain the best-preserved examples of old volcanic and sedimentary rocks (Lowe and Byerly, 1999; Arndt et al. 2008). The preservation of primary chemical and isotopic signatures during metamorphic recrystallization has been the subject of numerous studies for Barberton komatiites (e.g. Gruau et al., 1990, 1992; Lécuyer et al., 1994; Lahaye et al., 1995). One way to evaluate the degree of metamorphic resetting of isotope systematics is through the use of the isochron method. If the isochron age for a set of samples agrees with the age of the formation, the initial isotope composition can more convincingly be used as a proxy of the source composition. Short-lived radiogenic isotope systematics are less sensitive to post-crystallization modification that occurs after the extinction of the parent isotope and thus better record early Earth events. This is the case of the short-lived ^{146}Sm-^{142}Nd ($T_{1/2}$=103 Ma) system which records magmatic processes (melting/crystallization) during the Hadean.

Here we present new results on the ^{146}Sm-^{142}Nd isotope systematics of Barberton komatiites from the Komati Formation and surrounding sedimentary rocks (mudstone, sandstone) from the Fig Tree Group and Buck Reef cherts from the Kromberg Formation sampled during the International Continental Drilling Program (ICDP, Arndt et al., 2010). All these samples were analyzed previously for ^{147}Sm-^{143}Nd and ^{176}Lu-^{177}Hf systematics (Blichert-Toft et al., 2015; Garçon et al., 2017). Previous published combined studies of lithophile trace element isotope systematics (^{146}Sm,^{147}Sm-^{142,143}Nd and ^{176}Lu-^{176}Hf) on Barberton komatiitic lavas suggest a source with non-chondritic relative abundances of refractory lithophile elements, and that this source formed during the Hadean, as early as 4.4 Ga (Blichert-Toft et al., 2004; Puchtel et al., 2013). More recent ^{147}Sm-^{143}Nd and ^{176}Lu-^{177}Hf isotope studies of Barberton komatiites suggested that the komatiite source was characterized by subchondritic Sm/Nd and superchondritic Lu/Hf ratios (Blichert-Toft et al., 2015). This signature could result from the recycling of sediments in the mantle source of the komatiites or, alternatively, from the crystallization of a deep magma ocean (Blichert-Toft et al., 2015; Puchtel et al., 2016). In order to better understand the entire history of mantle processes at the origin of Barberton komatiites, results from the three systematics $^{146\text{-}147}$Sm-^{142,143}Nd and ^{176}Lu-^{176}Hf are discussed together.

2. SAMPLES ANALYZED IN THIS STUDY

Seven komatiites were selected from drill cores BARB1 and BARB2 obtained during the ICDP drilling project in the Komati Formation in the Onverwacht Group of the Barberton Belt (Arndt et al., 2010). A description of the samples is given in Coetze (2014) and Blichert-Toft et al. (2015). The seven selected samples have been previously analyzed for ^{176}Lu-^{176}Hf and ^{147}Sm-^{143}Nd systematics by Blichert-Toft et al. (2015). They all belong to the Al-depleted group as defined by Robin-Popieul et al. (2012): they have low Al/Ti, relatively high concentrations of incompatible elements and rare earth element patterns (REE) depleted in heavy REE with (Gd/Yb)n between 1.21 and 1.32 when normalized to the primitive mantle Gd/Yb ratio. Two samples classified as hyaloclastite (BARB1 GC/9 and BARB1 GC/34) have high loss of ignition (LOI = 13.1 and 10.1 wt%, respectively) whereas other samples have LOI in the range 1.8-7.5 wt%.

The komatiites of the Onverwacht Group are divided into seven formations and are overlain by the Fig Tree (3.26–3.23 Ga; Kröner et al., 1991; Byerly et al., 1996) and Moodies Groups (3.23-3.21 Ga; Heubeck et al., 2013) which mostly consist of conglomerate, sandstone, shale, banded chert, banded iron formation and dacitic volcanic rocks. In the subduction-accretion model for this region, the Fig Tree and Moodies Groups could represent the fill of an evolving foreland basin fed by the erosion products of an orogenic complex (Lowe and Byerly, 1999). The analyzed sediment samples are mudstones and sandstones from ICDP cores BARB 4 and BARB 5 drilled in the Mapepe formation of the Fig Tree group. Based on the major and trace element compositions of these sediments, 3 groups were defined: crustal detritus-rich, Si-rich, and Ca-Fe-rich sediments (Garçon et al., 2017). In addition, two samples of chert from ICDP core BARB 3 drilled in a basal member of the Kromberg Formation in the Onverwatch group (Buck reef cherts, 3.42 Ga; Kröner et al., 1991) were analyzed for ^{142}Nd in this study. All sediments were previously analyzed for ^{147}Sm-^{143}Nd and ^{176}Lu-^{176}Hf isotopic systematics by Garçon et al. (2017). The Si-rich sediments from Fig Tree and the cherts from Buck reef show unusually high ε^{176}Hf as required to explain the superchondritic Lu-Hf isotopic signatures of the Barberton

komatiites in the model involving sediment recycling in the mantle source of komatiites (Blichert-toft et al., 2015).

3. PREVIOUS ISOTOPE STUDIES OF BARBERTON KOMATIITES

Isotopic studies of Barberton komatiites have been undertaken for at least the last four decades including some of the earliest geochronological studies using the Sm-Nd system (Hamilton et al., 1979). Early Sm-Nd studies (Hamilton et al., 1979; Jahn et al., 1982, Gruau et al., 1990, 1992, Lecuyer et al., 1994, etc) found that initial $^{143}Nd/^{144}Nd$ ratios for the komatiites scattered considerably to both sub- and superchondritic values. More recent analyses by Puchtel et al. (2013, 2016) of carefully sampled, relatively fresh komatiites yielded internally consistent data. However these samples may have a very small range of parent/daughter ratios and the isochon method cannot be applied to make sure the isotopic systems have remained closed since the formation age of the komatiites (e.g. Schapenburg komatiites). A summary of $^{146,147}Sm$-$^{142,143}Nd$ and ^{176}Lu-^{176}Hf data obtained recently on komatiite samples from the Onverwacht Group (3.55 Ga Schapenburg belt, 3.48 Ga Komati formation, and 3.3 Ga Weltevreden) is presented in Figures 1 and 2. This includes ^{143}Nd and ^{176}Hf results previously analyzed by Blichert-toft et al. (2015) on the same samples as those analyzed for ^{142}Nd in this study (orange circles with red borders in Figures 1 and 2). All data on the ^{146}Sm-^{142}Nd systematics measured on Barberton komatiites are also presented.

3.1. ^{147}Sm-^{143}Nd systematics

Samples from the 3.48 Ga Komati (ICDP and outcrop samples, 45 whole-rocks samples in total) have initial $\varepsilon^{143}Nd$ between -4 and +4 but 60% of the samples have slightly positive initial $\varepsilon^{143}Nd$ up to +1 and the mean value of the 45 measurements is equal to +0.5 (Figure 1A). Blichert-Toft et al. (2015) report conflicting results for whole-rock komatiite samples and clinopyroxene separates. Initial $\varepsilon^{143}Nd$ calculated on clinopyroxene separated from two komatiite samples are negative (around -2) whereas a separate from a third sample gives a different value with $\varepsilon^{143}Nd$= +2. Whole-rock data scatter from -2 to +2 in core samples and from -4 to +4 in outcrop samples. Blichert-Toft et al. (2015) suggest that the negative initial $\varepsilon^{143}Nd$ measured

in the clinopyroxene separates is representative of the source and propose that at least part of positive values measured in whole-rock results from disturbance during later hydrothermal alteration or metamorphism. ICDP komatiite samples analyzed in this study for the ^{146}Sm-^{142}Nd systematics are presented in a ^{147}Sm-^{143}Nd isochron plot in Figure 3A (data from Blichert-Toft et al., 2015). With a MWSD value of 22.0, the regression yields a non-statistically significant result. However the ^{147}Sm-^{143}Nd age is in agreement with the accepted age of 3.48 Ga for this formation. The initial ε^{143}Nd calculated from the regression is +0.3±3.3 and individual samples range from -1.0 to 1.8 when recalculated at 3.48 Ga (mean value = +0.4±1.9, 2SD).

Komatiite samples from Schapenburg belt, a segment of the Barberton belt (3.55 Ga) yield initial ε^{143}Nd between +1.7 and +2.7 (Puchtel et al., 2016), and samples of slightly younger (3.3 Ga) Weltevreden komatiites have initial ε^{143}Nd from 0 to +2 (Blichert-Toft et al., 2015; Puchtel et al., 2013) (Figure 1).

3.2. ^{176}Lu-^{176}Hf systematics

The Komati Formation data scatter widely on a Lu-Hf isochron diagram with an MSWD of 122 for the whole dataset (Blichert-Toft et al., 2015). Considering only the samples from the IDCP drill cores reduces the isochron scatter considerably, but results in a young age (2941 ± 41 Ma, MSWD =30) and negative initial ε^{176}Hf of -1.5 ± 0.8. Calculating the initial ε^{176}Hf of the individual ICDP whole-rock measurements at the igneous age of 3.48 Ga provides a range from -3.2 to +3.9 with a mean value of +1.4 ± 3.5 (2SD) (Figure 1). The mean ε^{176}Hf considering outcrop samples is equal to +2.3 ± 3.9 (3 extreme values were removed, Blichert-Toft et al., 2015; Puchtel et al., 2013). In contrast, the initial ε^{176}Hf of three clinopyroxene separates from the komatiites ranged from +2.5 to +5.9 (Blichert-Toft et al., 2015), which overlaps with the initial ε^{176}Hf determined for the whole-rock samples from which these clinopyroxenes were separated, but contrasts with the negative initial ε^{143}Nd calculated for the same clinopyroxenes. Data obtained for the ^{176}Lu-^{177}Hf systematics for samples analyzed in this study are presented in Figure 3B (data from Blichert-Toft et al., 2015). The ^{176}Lu-^{177}Hf age calculated using all samples is clearly too young (3062 ± 70 Ma, cf. supplementary Figure 1). However the slope is strongly influenced

by sample GC/34A which has the lowest Lu/Hf ratio. Excluding this sample gives an older age of 3363 ± 213 Ma (MSWD = 4, Figure 3B) which is, within uncertainties, in agreement with the formation age of the studied komatiites.

Schapenburg and Weltreveden komatiites have strongly positive $\varepsilon^{176}Hf$ with mean values at +5.5 and +7, respectively (Figure 1).

3.3. ^{146}Sm-^{142}Nd systematics

Data for $^{142}Nd/^{144}Nd$ from Caro et al. (2006) and Putchel et al. (2013, 2016) for komatiites from the 3.48 Ga Komati Fm, 3.55 Ga Schapenburg belt and 3.27 Ga Weltevreden area are reported in Figure 2. Puchtel et al. (2016) report deficits in ^{142}Nd in the 3.55 Ga Schapenburg komatiites with a mean $\mu^{142}Nd$ of -4.9 ± 2.8 (2SD, 8 samples). In contrast, no clearly resolved deviation relative to the terrestrial standard has been reported so far in other Barberton komatiites. Among the four Komati Formation samples measured by Caro et al. (2006), two are classified as tholeiitic basalts and two as komatiitic basalts. The mean $\mu^{142}Nd$ for these samples is -0.7 ± 2.1 when calculated relative to the AMES Nd standard. Puchtel et al. (2013) obtained an average $\mu^{142}Nd$ of 0.0 ± 4.8 (2SD) for four other komatiites from the Komati Formation, and $\mu^{142}Nd$ of +2.2 ± 7.1 (2SD) for four Al-undepleted Weltevreden komatiites. A meta-tholeiite sample of the Komati Formation analyzed by Schneider et al. (2018) has a small deficit in ^{142}Nd with a $\mu^{142}Nd$ of -5.4 ± 3.7.

4. METHODS

Komatiite samples were digested and processed following the dissolution and chemical separation protocols developed by Boyet and Carlson (2005, 2006) and slightly modified by Rizo et al. (2011). Samples were dissolved using a 3:1 mixture of HF-HNO_3 ultra-pure acids within Savillex Teflon beakers and placed on the hotplate at 120 °C for 48 hours. To expel the fluorides, komatiites were treated with 7M HNO_3 and ultra-pure $HClO_4$. After evaporation to dryness, they were taken up in 6M HCl and replaced closed onto the hotplate at 90 °C. Once clear sample solutions in HCl were obtained, Nd fractions were separated using a three-step method: (i.) a cation-

exchange column –with AG50W-X8 resin– using 2.5M and 4M HCl to collect middle to light rare earth elements (REE) from the bulk rock; (ii.) two consecutive passes through pressurized cation-exchange columns using 2-methylactic acid (0.2M and pH = 4.7) to collect Nd and eliminate Ce with the majority of the Sm (and Pr), which together produce isobaric interferences on ^{142}Nd, ^{144}Nd, ^{148}Nd and ^{150}Nd. (iii.) Finally, separation was completed by using Ln-Spec resin (50-100 microns) with 0.2M HCl to purify the collected Nd and remove all the residual Sm. The reference basalt BHVO-2 was dissolved and purified using the same analytical protocol.

Sediments were dissolved in Savillex Teflon beakers using ammonium bifluoride (NH_4HF_2) at 230°C for 12 hours following the procedure described in Zhang et al., (2012). Here Ce is separated from other REE once it is oxidized to Ce^{4+}. Details on this technique are found in Garçon et al. (2018). The LREE cut was dissolved in 10N HNO_3 + 20 mM $NaBrO_3$. The concentrated nitric solution containing trivalent LREEs was eluted on Ln-Spec resin (50-100 μm) while Ce(IV) remained adsorbed on the column. This step was performed twice. The Nd cut was then processed through a fine Ln-Spec resin (25-50 μm) using 0.2N to 0.25N HCl as eluents to isolate Nd. Finally, the Nd cut was purified on a cation resin AG50W-X8 (200-400 mesh) using 2N HNO_3 and 2.5N to 6N HCl to remove the residual traces of Ba and $NaBrO_3$. Total procedural blanks for Nd were negligible (15 pg) given that typical sample sizes allowed separation of hundreds of ng of Nd.

The Nd isotopic composition was analyzed as positive metal ion (Nd^+) on the Thermo Scientific Triton Thermal Ionization Mass Spectrometers (TIMS) at the Laboratoire Magmas et Volcans (LMV) in Clermont-Ferrand (France) and at the Earth and Planets Laboratory in Washington D.C. (USA) using double zone-refined rhenium filaments. Measurements were carried out using a two-line acquisition procedure with 3 sec. pause between line 1 and line 2 in which the Faraday cups were centered successively on masses 145 and 143. Measurement corresponds to blocks of 20 cycles each with 8 sec. integration time using amplifier rotation for a total of 540 cycles. Measured Nd isotope ratios were corrected for mass fractionation using the exponential law and ^{146}Nd/^{144}Nd = 0.7219. Interferences coming from Ce at mass 142 and Sm at masses 144, 148, and 150 were measured at mass 140 and 147 for Ce and Sm, respectively. Most sediment samples were measured using a 4-line routine allowing the

measurements of all isotope ratios dynamically (Garçon et al., 2018). Calculations were performed offline using the Matlab routine presented in Garçon et al. (2018). Two dynamic $^{142}Nd/^{144}Nd$ ratios were obtained with this method and the average value is reported here. Each run was thoroughly examined and the four criteria described by Garcon et al. (2018) were applied. Ratios were corrected for the drift (fractionation rate) as described in Garçon et al. (2018) and the runs were stopped when $^{146}Nd/^{144}Nd$ reached 0.724. All results presented in Table 1 are runs characterized by normal, smooth and slow evolution of the $^{146}Nd/^{144}Nd$ ratio. The mass fractionation rate was always below the threshold limit of 0.4 ppm/s proposed by Roth et al. (2014).

Komatiite samples were measured in two different analytical sessions spaced 2 months apart. Sediments were measured during 5 sessions (#3 to #7). The terrestrial neodymium standard JNdi-1 was measured 4 to 10 times each session using the same acquisition procedure as for the samples (Table 1). The external reproducibility (2SD) on the $^{142}Nd/^{144}Nd$ ratio is between 3.5 and 6.2 ppm for these 7 sessions. A similar range is obtained on the other Nd isotope ratios, except for $^{150}Nd/^{144}Nd$ that is up to 31 ppm in session 6. The $^{143}Nd/^{144}Nd$ ratios measured for the JNdi-1 standard are in the range 0.512097 to 0.512104, in perfect agreement with the accepted value of 0.512099 ± 0.000005 (Garçon et al., 2018).

Samples (komatiites, sediments and BHVO-2) were measured between 1 and 5 times. They are either different measurements of the same load (called re-run in Table 1), different rhenium filaments (called re-load) or different dissolutions and chemical procedures of the same sample (called duplicate). Generally, $^{142}Nd/^{144}Nd$ isotope ratios measured on samples are expressed in μ-units ($\mu^{142}Nd = [(^{142}Nd/^{144}Nd)_{sample}/(^{142}Nd/^{144}Nd)_{JNdi\text{-}1})\text{-}1]\times10^{6}$) and calculated relative to the average value obtained for the JNdi-1 standard (assumed to be equal to the modern terrestrial value, $\mu^{142}Nd = 0$) in the given TIMS session. Results are compiled in Table 1 and plotted in Figure 2.

5. RESULTS

Komatiite samples have $\mu^{142}Nd$ values ranging from -2.2 ± 5.2 to -7.7 ± 2.8 (2SD) (Figure 2). These values are barely resolved from the JNdi-1 terrestrial standard when 2 SD uncertainties are considered, but all our samples have negative $\mu^{142}Nd$. Most of samples were measured several times and results are in good agreement. There is no correlation between Ce and Sm interferences and $^{142}Nd/^{144}Nd$ ratios. The average $\mu^{142}Nd$ for all komatiites is -4.0 (2SD = 4.1; 2SE = 1.5). The modern basalt from Hawaii, BHVO-2, has a $\mu^{142}Nd$ = -1.3 ± 3.9 and is thus not resolved from the JNdi standard value. We note that for 3 out of 7 samples, our measured $^{143}Nd/^{144}Nd$ ratios are in perfect agreement with those of Blichert-Toft et al. (2015) with a difference lower than 5 ppm. Compared to the data from Blichert-Toft et al. (2015), sample BARB1 GC/4 shows a difference of 64 ppm and the difference is even larger for BARB1 GC/34A, BARB2 GC/1 and GC/6 with differences of 159 ppm, -212 ppm and 493 ppm, respectively. Although we did not use the same dissolution technique (Parr bomb in Blichert-Toft et al. (2015) *vs*. Savillex beakers on hot plate in this study), the variable results are unlikely to be due to the mineralogy of these samples because komatiites are not expected to contain mineral phases that require high pressure and temperatures for dissolution. Results of incomplete sample dissolution have been highlighted by Blichert-Toft et al. (2004) for the Lu-Hf systematics where zircon would have a significant influence if it were present in the sample. Here we suspect instead a powder heterogeneity with variable amounts of secondary minerals like amphibole and titanite that are important REE carriers. A small change of 5% in the Sm/Nd ratio is sufficient to explain the largest difference in $^{143}Nd/^{144}Nd$ observed for BARB2 GC/6.

Our data for komatiites from ICDP cores BARB 1 and BARB 2 in the Komati Formation show deficits in ^{142}Nd. These, like the Schapenburg komatiites, are Al-depleted; they both display depletion in HREE relative to MREE ($1.3 < (Gd/Yb)_{N, CHUR} < 1.6$) associated with low Hf/Sm ratios (<0.6 compared to ≈ 0.7 for the Bulk Silicate Earth, Palme and O'Neil, 2014). Weltevreden komatiites, in contrast, are strongly depleted in LREE relative to HREE (Stiegler et al, 2012; Puchtel et al., 2013). The $^{142}Nd/^{144}Nd$ ratios expressed in μ-units show a positive correlation with Hf/Sm (Figure 4). Samples with the lowest $^{142}Nd/^{144}Nd$ ratios have the lowest Hf/Sm values, except sample BARB1 GC/34A which falls off of this correlation. GC/34A is

the hyaloclastite with the highest LOI (13.1 %). Its $^{176}Lu/^{177}Hf$ ratio is very low (0.01181) in comparison to other studied samples (0.02420-0.03075) (Blichert-Toft et al., 2015). These features suggest that the trace element compositional characteristics of this sample have been modified during metamorphism or hydrothermal alteration.

Sediments show a larger variability in $\mu^{142}Nd$ with reproducibility (2SD) exceeding 5 ppm for 7 samples (Table 1 and Figure 2). We interpret this variability as reflective of the fact that sediments contain components with distinct sources and hence powder heterogeneity would translate into variability in isotopic composition. This possibility is supported by the large variability seen in $^{143}Nd/^{144}Nd$ in different measurements of the same sample (see Table 1). Considering the average of all measurements performed for each sediment, none of the sediments show a resolved ^{142}Nd anomaly even if most of the values are negative. Similarly, when gathered by sediment types, none of the 4 groups (crustal detritus-rich sediments, Si-rich sediments, Ca-, Fe-rich sediments and cherts) show a resolvable ^{142}Nd anomaly. Crustal detritus-rich, Si-rich, Ca-Fe-rich sediments, and cherts have average $\mu^{142}Nd$ equal to 2.0 ± 7.3, -4.2 ± 10.1, -1.8 ± 4.2, 1.7 ± 12.6, respectively. Errors (2SD) are higher than those calculated on magmatic samples (komatiites and BHVO-2) and do not strictly reflect analytical error but mostly sample heterogeneity.

6. DISCUSSION

6.1. Sm-Nd and Lu-Hf systematics of komatiites do not support recycling of sedimentary material into the komatiite source

Komatiites from ICDP cores BARB1 and BARB2 (Komati Formation) have negative $\mu^{142}Nd$ values, a signature that reflects an early-formed source with subchondritic Sm/Nd ratio. Blichert-Toft et al. (2015) inferred a source with subchondritic Sm/Nd from the negative initial $\varepsilon^{143}Nd$ in the Komati clinopyroxene data but their whole rock initial $\varepsilon^{143}Nd$ data range from negative to positive values. In contrast, the majority of initial $\varepsilon^{176}Hf$ reported by Blichert-Toft et al. (2015) provides positive values, up to +5.9. These values are indicative of a source characterized by superchondritic Lu/Hf formed early in Earth's history. These results suggest a decoupling of the Sm/Nd and

Lu/Hf isotope systems compared to that expected for melting in the upper mantle and observed in most mantle-derived magmas throughout Earth history.

In a $\varepsilon^{176}Hf$-$\varepsilon^{143}Nd$ diagram, modern mantle-derived rocks such as mid-ocean ridge basalts and ocean island basalts - MORB and OIB - plot along a trend named the mantle array *i.e.* the Sm/Nd and Lu/Hf isotope systems are coupled. This positive correlation reflects the common behaviors of the daughter elements (Hf and Nd) that are more incompatible than the parents (Lu and Sm) during magmatic processes (melting, crystallization) occurring in the upper mantle. Chauvel et al. (2008) demonstrated that the slope of the mantle array is well reproduced by the melting of a depleted peridotitic source contaminated by old oceanic crust and sediments derived from the erosion of subaerial continental crust. Volcanic arc lavas tend to fall off this correlation because they have slightly more radiogenic Hf isotope ratios relative to MORB and OIB. This signature is caused by transfer during subduction of surface material (sediments or altered oceanic crust) into the mantle wedge where melting takes place (Chauvel et al., 2009). The major carrier of Hf in continental crust is zircon, a mineral particularly resistant to weathering. Weathering and erosion fractionate the Lu/Hf ratio such that fine-grained sediments have high Lu/Hf ratios due to selective removal of coarse-grained zircon. Over time, these sediments develop radiogenic Hf isotopic compositions but the Sm/Nd ratio is not modified because both elements are carried in the same mineral phases.

The nature of early crust (mafic vs. felsic) and the evolution of its composition through time are widely discussed (Carlson et al., 2019 and references therein). Erosion products of a mafic crust devoid of zircons should not record decoupling of parent/daughter ratios for the Sm-Nd and Lu-Hf isotope systematics. The study by Garçon et al. (2017) of Barberton metasedimentary rocks drilled in the Fig Tree Group provides a good overview of the composition of the eroded crust in the Barberton area. The Fig Tree Group is younger than the Komati komatiites, but contains sediments derived from crustal terranes that were present at the surface during komatiitic volcanism. Crustal detritus-rich sediments from Fig Tree (see Garçon et al., 2017) are the most suitable samples to estimate the composition of the crust in the Barberton area. They show no significant decoupling of their Sm-Nd and

Lu-Hf isotope systematics at the time of deposition. Therefore, the incorporation of such sediments alone into the komatiitic mantle source cannot explain the superchondritic Lu-Hf isotopic signatures measured in most Barberton komatiites (Figure 1B). In contrast, Si-rich sediments from Fig Tree have slightly negative $\varepsilon^{143}Nd$ (up to -2 at the time of deposition) and extremely radiogenic $\varepsilon^{176}Hf$ (up to +11). This composition reflects the presence of old chert clasts. Indeed, cherts from Buck Reef have very high $^{176}Lu/^{177}Hf$ (0.12-1.33) and extremely low Hf/Sm ratios (mean value 0.03, Garçon et al., 2017). Taken together, these two features may explain the radiogenic Hf signature and the unusually low Hf/Sm ratios of the Komati komatiites (Figures 1B and 4) if sediments similar to Buck Reef cherts were incorporated into the mantle source of the komatiites (cf. model of Blichert-Toft et al., 2015). Note that Buck Reef cherts are almost devoid of crustal detritus (i.e. no terrigenous input), and hence represent an extreme pure endmember of what could be an Archean seawater precipitate (Ledevin et al., 2019). The trace element patterns of cherts, in particular Buck Reef cherts, are very different from other types of sedimentary rocks because they have extremely low concentrations of REE and Hf (Figure 5). Because of the elemental mass balance, once these sediments are mixed with other types of sediments, the low Hf/Sm signature of cherts is rapidly overprinted by the more typical Hf/Sm ratios of crustal detritus-rich sediments. Assuming that the cores BARB-4 and BARB-5 are representative of sediments deposited on the seafloor, we estimate that Archean sediments recycled into the mantle would be made of about 31% Si-rich sediments, 24% Ca-, Fe-rich sediments, 34% crustal detritus-rich sediments and 10% cherts. The trace element pattern of such a mixture is shown in Figure 5. While cherts have a negative Hf anomaly, the mixture pattern displays a positive Hf anomaly and a higher Hf/Sm ratio (0.97) than the komatiites drilled in BARB-1 and BARB-2 (0.39-0.71). Assuming that Nd and Hf are congruently transferred from the surface to the melting region, recycling of this sediment mixture in the mantle cannot produce the trace element characteristics of the studied komatiites. Preferential extraction of rare earth elements such as Sm and Nd over high field strength elements (HFSE) such as Hf from the slab during subduction, as seen for example in calc-alkaline basalts from Newberry volcano (low Hf/Sm ratios, Carlson et al., 2018), would make things even worse since it would increase the Hf/Sm ratio of the recycled material transported into the deep mantle. The latter

process is not considered in the modeling presented below. The modelling also does not include crustal detritus-rich sediments and assumes that chert is the only type of sedimentary rocks being recycled into the source of the komatiites.

Blichert-Toft et al. (2015) attributed the decoupled Hf-Nd isotope signature to the incorporation of chert into the source of some Barberton komatiites. Modeling performed in our study does not support this conclusion. Blichert-Toft et al. (2015) modelled the Nd-Hf isotopic composition of komatiitic source as a mixture between cherts and peridotitic depleted mantle. We obtained divergent results because we include a third component, oceanic crust. If the recycling of sediments into the mantle occurred, it could be driven by plate tectonics and thus sediments would be subducted as a thin layer on top of the oceanic crust. This scenario is highly speculative but several geochemical evidences support initiation of plate tectonics on Earth shortly after the end of the Hadean (e.g. Shirey et al., 2008). We also considered two compositions for the mantle: primitive mantle and mantle depleted in incompatible elements with a composition similar to depleted MORB mantle. The end-member compositions are reported in Table 2 and plotted in Figure 6. We note that a Hf/Sm ratio as low as 0.6 as measured in the studied komatiites requires an unlikely high contribution of chert in the recycling material (crust-chert ratio of 40:60) with a minimum of 30% of recycling into the mantle i.e. melting of a source consisting of 70% peridotitic mantle and 30% crust-chert. Moreover a crust-chert ratio of 40:60 corresponds to an unrealistic thickness of 15 km of chert accumulated on top of 10 km of oceanic crust. Furthermore, magmas with the composition of komatiites cannot be produced by melting a source that enriched in SiO_2. This extreme scenario gives a maximum deficit of -3 ppm in $\mu^{142}Nd$, a $\varepsilon^{143}Nd$ of about -0.5 and a positive $\varepsilon^{176}Hf$ of about +2 assuming a depleted composition for the peridotitic mantle component (Figure 6). However, it does not explain the Hf/Sm - $\mu^{142}Nd$ correlation observed for Barberton komatiites as shown in Figure 4 (see mixing curves in Supplementary Figure 2).

These calculations show that the recycling of deep-sea sediments does not satisfy both the isotope constraints and the Hf/Sm ratio of the studied komatiites. Another mechanism of formation must therefore be envisaged to explain the $^{146,147}Sm$-$^{142,143}Nd$ and ^{176}Lu-^{176}Hf isotopic systematics of the studied komatiites.

6.2. Deep residual liquid of magma ocean crystallization in the komatiite source

As mentioned above, Sm-Nd and Lu-Hf fractionate in the same sense when melting or crystallization occur in the upper mantle. The two isotopic systems can however be decoupled when deep mantle mineral phases are involved (Figure 7A). Bridgmanite is the only abundant mantle mineral that preferentially concentrates Hf relative to Lu ($D_{Hf}>D_{Lu}$). We calculated the bulk partition coefficient for a mixture of bridgmanite/ferropericlase/Ca-perovskite in the proportions estimated for the lower mantle (Figure 7B). Sm/Nd and Lu/Hf are decoupled when the bridgmanite proportion exceeds 77% because at this point, the bulk partition coefficient for Lu becomes smaller than that of Hf, and Sm/Nd and Lu/Hf ratios are inversely fractionated during melting or crystallization. This signature has been identified from ^{176}Hf-^{143}Nd isotope measurements of Isua metabasalts from several formations and interpreted to reflect a deep magma ocean event (Rizo et al., 2011 Hoffman et al., 2011).

The following discussion explores the different steps that are needed in the fractionation history of the source of the Komati komatiites to explain their low Hf/Sm ratios together with their $^{142}Nd/^{144}Nd$, $^{143}Nd/^{144}Nd$, $^{176}Hf/^{177}Hf$ isotopic compositions (Table 3, Figures 8 and 9). We argue that the crystallization of a deep magma ocean plays a major role in the generation of the observed μ^{142}Nd-Hf/Sm correlation (Figure 4) even if melting and fractional crystallization processes that may occur during magma ascent during the last step can slightly modified the REE-Hf signature (Puchtel et al., 2016: Sossi et al., 2016). This model generally follows the different steps proposed by Puchtel et al. (2016) for Schapenburg komatiites.

Stage 1. CHUR evolution

During the first stage starting from the formation of the solar system, the primitive mantle has a chondritic composition.

Stage 2. Isotopic evolution of solidified magma ocean

Lu/Hf and Sm/Nd fractionated during crystallization of a deep magma ocean as represented in Figure 8. We used a model similar to model 1 of Morino et al. (2018) and the partition coefficients and other parameters are reported in Table 3. We calculated compositions of cumulate and residual melt at each step using a batch crystallization model. We consider a constant mineralogical assemblage over the crystallization interval proceeding from the bottom up. Melting diagrams show a sequence of crystallization at high pressure and for a BSE bulk composition establishing the normative abundances of bridgmanite, ferropericlase and Ca-perovskite (see the review by Andrault et al., 2017). Our calculations were made for a constant amount of ferropericlase (16%) and variable proportions of Ca-perovksite (2 to 7%) and bridgmanite (77 to 82%). These changes in proportions are first-order simulations of the progress of crystallization with bridgmanite alone in the early stages and higher proportions of Ca-perovskite in the later stages. The negative μ^{142}Nd and strongly positive initial ε^{176}Hf of Barberton komatiites reflects a source with low Sm/Nd and high Lu/Hf ratios (upper left quadrant in Figure 8). This signature corresponds to residual liquids formed by the crystallization of deep cumulates containing a relatively high proportion of Ca-perovskite. The compositions closest to the BSE values are produced in the first steps of the crystallization while the most extreme compositions correspond to 60% crystallization; i.e. solidification of the entire lower mantle.

If we assume an age for magma ocean crystallization, we can estimate Sm/Nd ratios for the komatiite source using the ^{142}Nd anomalies in Barberton samples. Fractionation ages calculated from combined ^{146}Sm-^{142}Nd and ^{147}Sm-^{143}Nd studies on Archean samples are mostly between 4.36 and 4.40 Ga (Boyet et al., 2003; Caro et al., 2003, 2016, Morino et al., 2018). Given that similar age ranges are obtained for samples from the lunar crust and for differentiation of the lunar mantle, this suggests that the terrestrial magma ocean crystallized shortly after the giant Moon-forming impact (Borg et al., 2019). During the second stage (T_1 from 4.36-4.40 Ga), we assume ^{147}Sm/^{144}Nd ratios between 0.175 to 0.190 and obtain a deficit of 5 ppm (+/- 3) for μ^{142}Nd.

529 The amount of bridgmanite needed to fractionate Sm/Nd ratios in this range has a
530 strong effect on the Lu/Hf ratios, as shown in Figure 8. Lu/Hf ratios are strongly
531 fractionated in residual liquids that form from a source with a high proportion of
532 bridgmanite; the Hf/Sm ratio decreases rapidly as the proportions of bridgmanite
533 increases. We consider it unlikely that liquid is trapped at the beginning of the
534 crystallization when the crystal fraction and the viscosity are both low (Solomatov,
535 2007). Our preferred model assumes an assemblage of 76% bridgmanite, 16%
536 ferropericlase and 5% of Ca-perovskite. After 30% of crystallization, the residual
537 liquid has the composition shown with the symbol 2 in Figure 8 and a Hf/Sm ratio
538 equal to 0.57 (Table 3) that is very similar to the mean Hf/Sm ratio of analyzed
539 samples (0.58 ±0.07 excluding BARB1 GC34/A). In our model, the crystallization of
540 bridgmanite/Ca-perovskite in the magma ocean lowers the Hf/Sm ratio of the source.
541 We show in the following section that this ratio also varies slightly during melting or
542 crystallization in the upper mantle.
543
544 **Stage 3. Depletion event in the upper mantle**
545 Considerable uncertainty surrounds the ^{147}Sm-^{143}Nd isotopic signature of the
546 komatiitic source at 3.48 Ga because whole-rock measurements scatter around
547 chondritic compositions while two out of three clinopyroxene separates have a
548 negative initial ε^{143}Nd of about -2 (Figure 1). Values of ε^{176}Hf of clinopyroxenes and
549 whole rocks, also calculated for the source at 3.48 Ga, are more coherent and yield an
550 initial ε^{176}Hf of about +2 (Blichert-Toft et al., 2015). To explain the decoupled
551 signature of the short-lived Sm-Nd systematics and the long-lived ^{176}Lu-^{176}Hf
552 systematics of the samples from the Komati Formation, we invoke a depletion event
553 that occurred sometime after the extinction of ^{146}Sm. A multistage evolution is even
554 more pronounced in the Schapenburg komatiites which have distinctly positive ε^{143}Nd
555 (+2.4) and ε^{176}Hf (+5.6) at 3.55 Ga (Puchtel et al., 2016), yet negative μ^{142}Nd (-5.5).
556
557 We invoke a low-degree (<1%) melting event after the extinction of ^{146}Sm (4 Ga).
558 This melting event would have depleted the mantle in incompatible elements to reach
559 a depletion degree similar that measured in modern N-MORB (i.e. less than 1% of
560 partial melting after Salters and Stracke, 2004). The mineralogy of the source is
561 estimated from melting models proposed by Salters and Stracke (2004) at 3 GPa

(garnet in the source). The composition of the solid residues left after extraction of a 0.5% partial melt is indicated by the symbol 3 in Figure 8. The initial ε^{143}Nd value in this model is always negative (Figure 9) which is consistent with the negative value measured in the Barberton clinopyroxene separate but inconsistent with the near-zero values obtained from the whole rock samples. A small increase of the degree of partial melting (1%) gives initial ε^{143}Nd and ε^{176}Hf equal to 0 and 2.2, respectively. The source of Schapenburg komatiite may have experienced a higher degree of partial melt extraction (5% for Schapenburg komatiites) producing highly radiogenic values at 3.55 Ga (Figure 1). The Hf/Sm ratio of the mantle source is not significantly modified during this melting event (see Table 3).

Stage 4. Melting to produce the komatiite magmas

After the depletion event, the komatiites formed at 3.48 Ga by decompression melting during which majorite was left in the residue. As shown in Figure 8 the Sm/Nd and Lu/Hf ratios of Komati and Schapenburg komatiites are perfectly reproduced considering 30% partial melting of a source comprising 55% olivine and 45% majorite, which corresponds to the mineralogy of deepest part of the upper mantle (18-22 GPa, Morino et al., 2018). The model well reproduces the negative μ^{142}Nd and the positive initial ε^{176}Hf for komatiites at 3.48 Ga (Figure 9). We obtain a slightly negative ε^{143}Nd value at 3.48 Ga, which is intermediate between with the negative initial ε^{143}Nd recorded by the clinopyroxene separates and the near zero value of the whole rocks. Ratios calculated at each step are reported in Table 3. The final Hf/Sm value is slightly lower than those measured in komatiites (0.51 instead of 0.58) but remains in good agreement with the measured ratios when considering model uncertainties (see below and Figure 10).

Because we do not know the exact timing of the different events and the compositions of the different reservoirs involved in the isotopic model described above, we performed a Monte-Carlo simulation (N = 10, 000) assuming variable input parameters at each stage (Figure 10) to test the robustness and sensitivity of the model. In Stage 1, we took into account the uncertainty on the initial Sm-Nd and Lu-Hf isotopic composition of the Bulk Silicate Earth (uncertainty on the ^{176}Lu/^{177}Hf and ^{147}Sm/^{144}Nd ratios of the CHUR from Bouvier et al., 2008). In Stage 2, we assumed

595 that the magma ocean crystallized between 4.36 and 4.40 Ga as discussed above. As
596 we do not precisely know how much of the mantle crystallized, we let the percentage
597 of crystallization vary between 20 and 50% with a range of composition for the
598 cumulate as shown in Figure 9 (bridgmanite/ferropericlase/Ca-perovskite from
599 77/16/7 to 82/16/2). In Stage 3, we tested the effects of changing the depletion age
600 between 4.1 and 3.9 Ga and a melting fraction between 0.2 and 1.2% for the mantle
601 depletion event. Finally, in Stage 4, we let the melt fraction vary between 30 and 40%
602 to form the komatiite at 3.48 Ga. Using these ranges of parameters for each stage
603 rather than a fixed value show that the results of the komatiite model are consistent
604 with the measured values.
605 The Monte-Carlo simulation perfectly reproduces the range of $^{147}Sm/^{144}Nd$,
606 $^{176}Lu/^{177}Hf$, and Hf/Sm ratios measured in the studied komatiites (Figure 9). The
607 modelled initial Nd and Hf isotopic composition are within the range of those
608 measured in the komatiites but are under constrained given the wide range of input
609 parameters we used for each stage in the Monte-Carlo simulation (Figure 10). More
610 importantly, we performed several other Monte-Carlo simulations (not shown here)
611 involving melting events only in the upper mantle (i.e. replacing the magma ocean
612 crystallization stage by an early melting event in the upper mantle) and none of them
613 was successful in reproducing the decoupled Nd-Hf isotopic signature of the studied
614 komatiites. Finally, we note that the results of the model are highly sensitive to the
615 partition coefficients used for the melting and crystallization event at each stage. We
616 thus tried to carefully select the most appropriate partition coefficients (mineral
617 assemblages, pressure and temperature similar to those expected for the modeled
618 processes). The sources of the model parameters, including partition coefficients, are
619 reported in Table 3.
620
621 The correlation observed between $\mu^{142}Nd$ and Hf/Sm in komatiites suggests that the
622 fractionation of Hf from Sm occurred during an early event. Only the crystallization
623 of lower mantle mineral phases fractionates enough the high field strength elements
624 from the rare earth elements. Modeling of the magma ocean crystallization shows that
625 Hf/Sm fractionation remains relatively weak in the residual liquid in comparison to
626 the cumulate (see trace element patterns in supplementary Figure 3), hence it is
627 expected that the trace element pattern of the studied komatiites should not record a

strong magma ocean signature. Anomalies in HFSE can be quantified using the Zr anomaly $Zr/Zr^*=Zr_N/(Sm_N+Nd_N)/2)$ with $_N$=normalized to CI (Barrat et al., 2012). The Zr anomaly calculated in the residual melt (0.78 in stage 2) is lower than that measured in Schapenburg and Komati komatiites (0.53 to 0.61), suggesting that the komatiites may have indeed preserved the remnant signature of the magma ocean crystallization event.

In contrast, the Weltevreden komatiites source does not retain a record of the deep magma ocean crystallization event. Zirconium anomalies are weaker in the samples (0.82 to 0.93) in good agreement with their higher Hf/Sm ratios and the absence of a resolved ^{142}Nd anomaly. The trace elements in these komatiites record a strong depletion event that occurred sometime before or during the melting that produced the komatiite magma. This event decreases only slightly the Hf/Sm ratio.

Schapenburg komatiites have higher εHf and ε^{143}Nd at the age of crystallization relative to Barberton komatiites. Puchtel et al. (2016) propose that the source was depleted by 5% partial melting in Stage 3. In this case, the depletion event completely erases any magma ocean crystallization signature recorded by the long-lived isotopes. This emphasizes the value of measuring the short-lived ^{146}Sm-^{142}Nd system when reconstructing events in the Hadean and Archean mantle.

7. Conclusions

Measurements of ^{146}Sm-^{142}Nd systematics in komatiites and sediments sampled during the ICDP drilling project (BARB1-2-3-4-5) give strong constraints on the evolution of the mantle source through time. The resolved negative μ^{142}Nd measured in komatiites prove that the source was fractionated early in Earth history to form a reservoir with a subchondritic Sm/Nd ratio. Deficits in ^{142}Nd are correlated with low Hf/Sm ratios suggesting that fractionation between rare earth elements and high field strength elements occurred during this early differentiation event. These komatiites have strongly radiogenic initial ε^{176}Hf, but near-chondritic initial ε^{143}Nd indicated decoupling of Sm-Nd and Lu-Hf systematics. As previously proposed for

Schapenburg komatiites, which share similar geochemical characteristics (deficit in ^{142}Nd, radiogenic $\varepsilon^{176}Hf$), the mantle source recorded the crystallization of a deep magma ocean. We calculate that the komatiite mantle source represents the residual liquid for a bridgmanite/ferropericlase/Ca-perovskite mineralogy in proportion 79/16/5 after 50% crystallization of the lower mantle. Melting under these conditions decouples Lu-Hf from Sm-Nd, and lowers the Hf/Sm ratio. Parent/daughter ratios were fractionated again during a depletion event that occurred after the extinction of ^{146}Sm. With this model we explain the positive $\varepsilon^{176}Hf$ and chondritic to slightly subchondritic $\varepsilon^{143}Nd$, negative $\mu^{142}Nd$ and low Hf/Sm ratios measured in the komatiitic samples. Recycling of chert cannot explain both the Hf and Nd isotopic systematics of Barberton komatiites. None of the sediments measured in the Barberton area have significantly negative ^{142}Nd and the recycling of these sediments does not change the Hf/Sm ratio of the mantle source.

ACKNOWLEDGMENTS

We acknowledge the International Continental Scientific Drilling Program (ICDP; http://barberton.icdp-online.org) for providing samples. We are grateful to Chantal Bosq and Mary F. Horan for ensuring optimal working conditions in the clean laboratory, and to Jean-Luc Piro, Delphine Auclair, and Timothy D. Mock for help with the mass spectrometers. We thank Denis Andrault and Julien Monteux for constructive discussions. We also thank Janne Blichert-Toft for editorial handling, Klaus Mezger, Igor Puchtel and Guillaume Caro for their constructive comments. This study has received funding from Carnegie Institution for Science, the French Government Laboratory of Excellence initiative n°ANR-10-LABX-0006, the Région Auvergne, and from the European Union's Horizon 2020 research and innovation programme under Grant Agreement N° 682778. This is Laboratory of Excellence ClerVolc contribution number XXX.

REFERENCES

693 Andrault D., Bolfan-Casanova N., Bouhifd M. A., Boujibar A., Garbarino G.,
694 Manthilake G., ... and Pesce G. (2017) Toward a coherent model for the melting
695 behavior of the deep Earth's mantle. *Physics of the Earth and Planetary*
696 *Interiors 265*, 67-81.
697 Arndt N. T., Lesher C. M. and Barnes S. J. (2008). Komatiite. Cambridge University
698 Press, Cambridge, 487pp; chapter 13.
699 Arndt N.T., Wilson A., Hofmann A., Mason P., Bau,M., Byerly G., and Chunnett G.
700 (2010) Scientific drilling in the Barberton Greenstone Belt. *Geobulletin* 53, 17–
701 18.
702 Barrat J. A., Zanda B., Moynier F., Bollinger C., Liorzou C. and Bayon G. (2012)
703 Geochemistry of CI chondrites: Major and trace elements, and Cu and Zn
704 isotopes. *Geochimica et Cosmochimica Acta*, *83*, 79-92.
705 Blichert-Toft J., Arndt N. T. and Gruau G. (2004) Hf isotopic measurements on
706 Barberton komatiites: effects of incomplete sample dissolution and importance
707 for primary and secondary magmatic signatures. *Chemical Geology* 207, 261-
708 275.
709 Blichert-Toft J., Arndt N. T., Wilson A. and Coetzee G. (2015) Hf and Nd isotope
710 systematics of early Archean komatiites from surface sampling and ICDP
711 drilling in the Barberton Greenstone Belt, South Africa. *American Mineralogist*
712 100, 2396-2411.
713 Borg L. E., Gaffney A. M., Kruijer T. S., Marks N. A., Sio C. K. and Wimpenny, J.
714 (2019) Isotopic evidence for a young lunar magma ocean. *Earth and Planetary*
715 *Science Letters 523*, 115706.
716 Bouvier A., Vervoort J. D. and Patchett P. J. (2008) The Lu–Hf and Sm–Nd isotopic
717 composition of CHUR: constraints from unequilibrated chondrites and
718 implications for the bulk composition of terrestrial planets. *Earth and Planetary*
719 *Science Letters 273*(1-2), 48-57.
720 Bouvier A. and Boyet M., (2016) Primitive solar system materials and Earth share a
721 common initial ^{142}Nd abundance. *Nature* 537, 399-402.
722 Boyet M., Blichert-Toft J., Rosing M., Storey M., Télouk,P. and Albarède, F., (2003)
723 ^{142}Nd evidence for early Earth differentiation. *Earth and Planetary Science*
724 *Letters* 214, 447-442.
725 Boyet M., and Carlson R. W., (2005) ^{142}Nd evidence for early (>4.53 Ga) global
726 differentiation of the silicate Earth. *Science* 309, 576-581.

727 Boyet M., and Carlson R.W., 2006. A new geochemical model for the Earth's mantle
728 inferred from ^{146}Sm-^{142}Nd systematics. *Earth Planetary Science Letter*s 250,
729 254-268.
730 Burkhardt C., Borg L. E., Brennecka G. A., Shollenberger, Q. R., Dauphas N. and
731 Kleine, T. (2016) A nucleosynthetic origin for the Earth´s anomalous ^{142}Nd
732 composition. *Nature* 537, 394-397.
733 Byerly G. R., Kröner A., Lowe D. R. and Todt W. (1996) Prolonged magmatism and
734 time constraints for sediment deposition in the early Archean Barberton
735 greenstone belt: evidence from the Upper Onverwacht and Fig Tree groups.
736 *Precambrian Research* 78, 125‑138.
737 Carlson R. W., Grove T. L. and Donnelly-Nolan J. M. (2018) Origin of Primitive
738 Tholeiitic and Calc-Alkaline Basalts at Newberry Volcano, Oregon.
739 *Geochemistry, Geophysics, Geosystems 19*(4), 1360-1377.
740 Carlson R. W., Garçon M., O'Neil J., Reimink J. and Rizo, H. (2019) The nature of
741 Earth's first crust. *Chemical Geology 530*, 119321.
742 Caro G., Bourdon, B. Birck, J.-L. and Moorbath, S., (2003) ^{146}Sm–^{142}Nd evidence
743 from Isua metamorphosed sediments for early differentiation of the Earth's
744 mantle. *Nature* 423, 428–432.
745 Caro G., Bourdon B., Birck J.L., and Moorbath S. (2006) High-precision ^{142}Nd/^{144}Nd
746 measurements in terrestrial rocks: constraints on the early differentiation of the
747 Earth's mantle. *Geochimica et Cosmochimica Acta* 70, 164-191.
748 Caro G., Morino P., Mojzsis S. J., Cates N. L., and Bleeker, W. (2017). Sluggish
749 Hadean geodynamics: Evidence from coupled 146,147 Sm–142,143 Nd
750 systematics in Eoarchean supracrustal rocks of the Inukjuak domain (Québec).
751 *Earth and Planetary Science Letters*, *457*, 23-37.
752 Chauvel C., Marini J. C., Plank T., and Ludden J. N. (2009) Hf-Nd input flux in the
753 Izu‑Mariana subduction zone and recycling of subducted material in the
754 mantle. *Geochemistry, Geophysics, Geosystems 10*(1).
755 Chauvel C., Lewin E., Carpentier M., Arndt N. T. and Marini J. C. (2008). Role of
756 recycled oceanic basalt and sediment in generating the Hf–Nd mantle array.
757 *Nature geoscience*, *1*(1), 64.

758 Coetzee G. (2014) Petrology and geochemistry of the Tjakastad (Barberton) ICDP
759 cores (Doctoral dissertation, University of the Witwatersrand, Faculty of
760 Science, School of Geology).
761 Corgne A., Liebske C., Wood B. J., Rubie D. C. and Frost D. J. (2005) Silicate
762 perovskite–melt partitioning of trace elements and geochemical signature of a
763 deep perovskitic reservoir. *Geochimica et Cosmochimica Acta* 69, 485–49.
764 Friedman A. M., Milsted J., Metta D., Henderson D., Lerner J. and Harkness A. L.,
765 Op, D.R. (1966) Alpha Decay Half Lives of ^{148}Gd ^{150}Gd and ^{146}Sm.
766 *Radiochimica Acta 5*(4), 192-194.
767 Garçon M., Carlson R.W., Shirey S.B., Arndt N.T., Horan M.F., Mock T.D. (2017)
768 Erosion of Archean continents: the Sm-Nd and Lu-Hf isotopic record of
769 Barberton sedimentary rocks. *Geochimica et Cosmochimica Acta*,206, 216-235.
770 Garçon M., Boyet M., Carlson R. W., Horan M. F., Auclair D. and Mock T. D. (2018)
771 Factors influencing the precision and accuracy of Nd isotope measurements by
772 thermal ionization mass spectrometry. *Chemical Geology* 476, 493-514.
773 Gruau G., Chauvel C. and Jahn B. M. (1990) Anomalous Sm-Nd ages for the early
774 Onverwacht Group volcanics: Significance and petrogenetic implications.
775 *Contributions to Mineralogy and Petrology* 104. 27-34.
776 Gruau G., Tourpin S., Fourcade S. and Blais S. (1992) Loss of isotopic (Nd, O) and
777 chemical (REE) memories during metamorphism of komatiites: New evidence
778 from eastern Finland. *Contributions to Mineralogy and Petrology*, 112. 66-82.
779 Hamilton P. J., Evensen N. M., O'nions R. K., Smith H. S. and Erlank, A. J. (1979).
780 Sm–Nd dating of Onverwacht Group Volcanics, southern Africa. *Nature*,
781 *279*(5711), 298-300.
782 Heubeck C., Engelhardt J., Byerly G. R., Zeh A., Sell B., Luber T. and Lowe D. R.,
783 (2013) Timing of deposition and deformation of the Moodies Group (Barberton
784 Green-stone Belt, South Africa): very-high-resolution of Archaean surface
785 processes. *Precambrian Research* 231, 236–262.
786 Herzberg, C. (1992) Depth and degree of melting of komatiites. *J. Geophysical*
787 *Research* 97, 4521-4540.
788 Hoffmann J. E., Münker C., Polat A. , Rosing M. T. and Schulz T., (2011) The origin
789 of the decoupled Hf-Nd isotope compositions in Eoarchean rocks from southern
790 West Greenland. *Geochiminica and Cosmochimica Acta* 75, 6610–6628.

791 Jahn, B.M., Gruau, G., Glikson, A.Y. (1982). Komatiites of the Onverwacht Group,
792 S. Africa: REE geochemistry, Sm/Nd age and mantle evolution. *Contributions*
793 *to Mineralogy and Petrology*, *80*(1), 25-40.
794 Kröner A., Byerly G. R. and Lowe, D. R. (1991) Chronology of early Archaean
795 granite-greenstone evolution in the Barberton Mountain Land, South Africa,
796 based on precise dating by single zircon evaporation. *Earth and Planetary*
797 *Science Letters 103*(1-4), 41-54.
798 Lahaye Y., Arndt N., Byerly G., Chauvel C., Fourcade S. and Gruau, G. (1995) The
799 influence of alteration on the trace-element and Nd isotopic compositions of
800 komatiites. *Chemical Geology 126*(1), 43-64.
801 Lécuyer C., Gruau G., Anhaeusser C. R. and Fourcade S. (1994) The origin of fluids
802 and the effects of metamorphism on the primary chemical compositions of
803 Barberton komattites: New evidence from geochemical (REE) and isotopic (Nd,
804 O, H, $^{39}Ar/^{40}Ar$) data. *Geochimica et Cosmochimica Acta* 58, 969-984.
805 Ledevin M., Arndt N., Chauvel C., Jaillard E. and Simionovici, A. The Sedimentary
806 Origin of Black and White Banded Cherts of the Buck Reef, Barberton, South
807 Africa. *Geosciences* 2019, 9, 424.
808 Lowe D. R. and Byerly, G. R. (1999) Geologic Evolution of the Barberton Greenstone
809 Belt, South Africa, Geological Society of America - Special Paper 329.
810 Morino P., Caro G., Reisberg L. (2018) Differentiation mechanisms of the early
811 Hadean mantle: insights from combined ^{176}Hf-$^{142,143}Nd$ signatures of Archean
812 rocks from the Saglek Block. *Geochimica et Cosmochimica Acta 240*, 43-63.
813 O'Neil J., Francis,D. and Carlson, R. W. (2011) Implications of the Nuvvuagittuq
814 greenstone belt for the formation of Earth's early crust. *Journal of Petrology*
815 *52*(5), 985-1009.
816 O'Neil J., Carlson R. W., Francis D. and Stevenson R. K. (2008) Neodymium-142
817 evidence for hadean mafic crust. *Science* 321, 1828-1831.
818 Ohtani, E. (1984) Generation of komatiite magma and gravitational differentiation in
819 the deep upper mantle. *Earth and Planetary Science Letters*, 67, 261-272.
820 Palme H. and O'Neill H. St. C. (2014) Cosmochemical Estimates of Mantle
821 Composition. In *Treatise on Geochemistry*, (Elsevier), 1–39.
822 Puchtel I. S., Blichert-Toft J., Touboul M., Walker R. J., Byerly G. R., Nisbet E. G.
823 and Anhaeusser C. R. (2013) Insights into early Earth from Barberton

824 komatiites: Evidence from lithophile isotope and trace element systematics.
825 *Geochimica et Cosmochimica Acta*, 108, 63-90.
826 Puchtel I. S., Blichert-Toft J., Touboul M., Horan M. F. and Walker R. J. (2016) The
827 coupled ^{182}W-^{142}Nd record of early terrestrial mantle differentiation.
828 *Geochemistry, Geophysics, Geosystems* 17(6), 2168-2193.
829 doi:10.1002/2016GC006324.
830 Rizo H., Boyet M., Blichert-Toft J. and Rosing M.T. (2011). Combined Nd and Hf
831 isotope evidence for deep-seated source of Isua lavas. *Earth and Planetary*
832 *Science Letters* 312, 267-279.
833 Robin-Popieul C.M., Arndt N.T., Chauvel C., Byerly G., Sobolev A. and Wilson A.
834 (2012). A new model for Barberton komatiites: deep critical melting with high
835 Roth A. S., Scherer E. E., Maden C., Mezger K., Bourdon, B. (2014). Revisiting the
836 142Nd deficits in the 1.48 Ga Khariar alkaline rocks, India. *Chemical geology*,
837 *386*, 238-248.
838 Salters, V. J. and Stracke, A. (2004). Composition of the depleted mantle.
839 *Geochemistry, Geophysics, Geosystems*, *5*(5).
840 Scherer E., Münker C. and Mezger K. (2001). Calibration of the lutetium-hafnium
841 clock. *Science*, *293*(5530), 683-687.
842 Schneider K. P., Hoffmann E., Boyet M., Münker C. and Kröner A. (2018)
843 Coexistence of enriched and modern-like ^{142}Nd signatures in Archean igneous
844 rocks of the eastern Kaapvaal Craton, southern Africa. *Earth and Planetary*
845 *Science Letters* 487, 54-66.
846 Shirey S. B., Kamber, B. S., Whitehouse M .J., Mueller P. A., Basu, A. R. (2008) A
847 review of the isotopic and trace element evidence for mantle and crustal
848 processes in the Hadean and Archean. The Geological Society of America,
849 Special Papers 440, 1-29.
850 Solomatov V. S. (2007) Magma oceans and primordial mantle differentiation.
851 *Treatise on geophysics 9*, 91-120.
852 Sossi P. A., Eggins S. M., Nesbitt R. W., Nebel O., Hergt J. M., Campbell I. H., ...
853 and Davies D. R. (2016). Petrogenesis and geochemistry of Archean komatiites.
854 *Journal of Petrology*, *57*(1), 147-184.
855 Stiegler M. T., Cooper M., Byerly G. R. and Lowe D. R. (2012) Geochemistry and
856 petrology of komatiites of the Pioneer Ultramafic Complex of the 3.3 Ga

857 Weltevreden Formation, Barberton greenstone belt, South Africa. *Precambrian*
858 *Research 212*, 1‑12.
859 Vervoort J. D. and Blichert-Toft J. (1999) Evolution of the depleted mantle: Hf
860 isotope evidence from juvenile rocks through time. *Geochimica et*
861 *Cosmochimica Acta 63*(3-4), 533-556.
862 Walter M. J., Nakamura N., Tronnes R .G. and Frost D. J., (2004) Experimental
863 constraints on crystallization differentiation in a deep magma ocean.
864 *Geochimica et Cosmochimica Acta* 68, 4267–4284.
865 Zhang W., Hu Z., Liu Y., Chen H., Gao S. and Gaschnig R. M. (2012) Total rock
866 dissolution using ammonium bifluoride (NH_4HF_2) in screw-top Teflon vials: A
867 new development in open-vessel digestion. *Analytical Chemistry* 84, 10686-
868 10693.

TABLE CAPTION

Table 1. Nd isotopic composition measured in komatiites and sediments drilled at BARB 1-5.

Table 2. Composition of the different end-members considered in the mixing model calculation. The composition of the Primitive Mantle is from Palme and O'Neill (2014). This mantle has chondritic ratios for refractory lithophile elements (Sm, Nd, Lu, Hf) and then has epsilon values at zero. The Depleted MORB Mantle composition is from Salters and Stracke (2004). Hf and Nd isotopic compositions have been calculated to account for an ε^{143}Nd value of +2 at 3.48 Ga (mean value measured in Archean samples, see Boyet and Carlson 2005). The Hf isotopic composition is then estimated using the Hf-Nd mantle array of Chauvel et al. (2008). This equation defined from modern samples is also valid for Archean samples (Vervoort and Blichert-Toft, 1999). A mafic rock from the Ujaraaluk unit from the Nuvvuagittuq Greenston Belt (sample PC-162 belonging to the enriched low-Ti group) is taken as an early crust analogue characterized by negative μ^{142}Nd (O'Neil et al., 2011). Hf and Nd isotopic compositions have been calculated considering the crust formed 4.3 Ga from a chondritic composition (O'Neil et al., 2008). Then the isotopic composition evolved until 3.45 Ga with parent/daughter ratios equal to those measured in the sample PC-162. Concentrations and parent/daughter ratios for chert correspond to the mean value of the 3 chert samples measured in Garçon et al. (2017). Hf-Nd isotopic compositions are calculated assuming an initial chondritic ratio and 0.8 Ga of evolution using the measured parent/daughter ratios. Cherts have extremely high Lu/Hf ratios and then develop with time highly radiogenic ^{176}Hf/^{177}Hf ratios. It is assumed that archean sediments on the oceanic seafloor have a residence time much higher than today (up to 200 Ma).

Table 3. Description of the 4-stage model explaining the ^{142,143}Nd and ^{176}Hf isotope signature of the komatiite source at 3.48 Ga and measured Sm/Nd, Lu/Hf and Hf/Sm ratios. For each step are reported 1) the timing, 2) partition coefficients and mineralogy of the source, 3) crystallization and melting rates.

Concentrations for the primitive mantle are from Palme and O'Neill (2014). Partition coefficients are from: Ca-perovskite and brigdminite (Corgne et al., 2005),

ferropericlase (Walter et al., 2004), olivine, orthopyroxene, clinopyroxene and garnet (compilation from Salters and Stracke 2004), majorite (compilation from Morino et al., 2018).

FIGURE CAPTION

Figure 1. Initial $\varepsilon^{143}Nd$ (**A**) and $\varepsilon^{176}Hf$ (**B**) for Schapenburg (3.55 Ga), Komati (3.48 Ga, ICDP samples are shown with red circles and outcrop samples with white triangles), and Weltevreden (3.33 Ga) komatiites. Data from Blichert-Toft et al. (2015) and Puchtel et al (2013, 2016). ICDP samples analyzed in this study are shown by symbols with red borders. Few samples with extremes values plotting outside of the scale are not represented. Cpx and Amph stand for clinopyroxene and amphibole separates respectively.

Figure 2. $\mu^{142}Nd$ ($^{142}Nd/^{144}Nd$ ratio normalized to terrestrial standard $x10^6$) measured in komatiite and sediment samples from the IDCP BARB 2-5 drilled cores. Most of samples were measured several times and the average value for each sample is represented by the symbol with larger border. Error bars are 2SE for individual measurement and 2SD for the mean value. The reference basalt BHVO-2 was measured 4 times yielding a mean value of -1.3 ± 3.9. Literature data on komatiites (Caro et al., 2006; Puchtel et al., 2013, 2014) and meta-tholeiite of the Komati Formation and two meta-komatiites from the Dwalile Greenstone Remnant (Schneider et al., 2018) are reported in the upper part of the diagram. The two grey fields correspond to average 2SD (dark) and 2SE (light) values calculated from repeated measurements of the JNdi-1 standard reported in Table 1.

Figure 3. Sm-Nd (**A**) and Lu-Hf (**B**) isochron diagrams for drill core komatiites (BARB 1 and BARB 2) analyzed in this study. Data are from Blichert-Toft et al. (2015).

Figure 4. $\mu^{142}Nd$ vs Hf/Sm in komatiites from Barberton (ICDP this study and Komati from Puchtel et al., 2013), Schapenburg (Puchtel et al., 2016) and

Weltevreden (Puchtel et al., 2013).). The two grey fields correspond to average 2SD (dark) and 2SE (light) values calculated from repeated measurements of the JNdi-1 standard reported in Table 1.

Figure 5. REE-Hf element patterns normalized to chondrites CI (Barrat et al., 2012) for sediments drilled in the Barberton area. Sediments have been analyzed in Garçon et al. (2017). The 4 groups are defined on the basis of major and trace elements. The red line entitled mixing represents a potential pile of sediments subducted during the Archean. Proportions are defined from the BARB 3-4-5 drilled core lithologies: 31% Si-rich sediments, 24% Ca-,Fe-rich sediments, 34% crustal detritus-rich sediments and 10% cherts. The composition of ICDP komatiites analyzed in this study are represented by the yellow field (Coetzee, 2014)

Figure 6. Evolution of the modeled $\mu^{142}Nd$ (**A**), Hf/Sm (**B**), $\varepsilon^{143}Nd_{3.48Ga}$ (**C**), and $\varepsilon^{176}Hf_{3.48Ga}$ (**D**) with respect to the sedimentary proportions determined using the mixing models. Values considered for the different end-members are reported in Table 2. Blue and black lines represent calculated mixing considering a primitive mantle compositions and a depleted mantle composition, respectively. This model assumes the recycling of a mafic crust with sediments at its top (pile of cherts). The crust/chert ratio gradually decreases from the plain line to the increasingly fine dotted lines (90:10, 70:30, 50:50, 40:60). These ratios mimic a difference in thickness and/or productivity during partial melting. The red line in the 4 panels shows the mean value measured in the studied komatiites. Initial $\varepsilon^{143}Nd$ and $\varepsilon^{176}Hf$ values are from Blichert-Toft et al., 2015. Initial $\varepsilon^{176}Hf$ values are positive for both clinopyroxenes and their host rocks (mean value = +3).

Figure 7. A) Mineral-melt partition coefficients for upper (clinopyroxene, orthopyroxene, olivine, majorite, garnet) and lower mantle phases (ferropericlase, Ca-perovskite, bridgmanite). Partition coefficients are from: Ca-perovskite and bridgmanite (Corgne et al., 2005), ferropericlase (Walter et al., 2004), olivine, orthopyroxene, clinopyroxene and garnet (compilation from Salters and Stracke 2004), majorite (compilation from Morino et al., 2018). Values for olivine and its polymorphs are not shown because the partition coefficients for these minerals are

extremely low ($<10^{-3}$), thus these phases do not contribute to the total budget of Sm, Nd, Lu, and Hf. **B**) Bulk partition coefficients for lower mantle mineralogy with bridgmanite/ferropericlase/Ca-perovskite proportions varying from 75/16/9 to 82/16/2. Sm/Nd and Lu/Hf fractionate in opposite directions when the bridgmanite proportion in the lower mantle is higher than 77% (dashed lines; or equivalent to a bridgmanite proportion higher than 92% in a bridgmanite/Ca –pervoskite two component mixing).

Figure 8. Present day $^{176}Lu/^{177}Hf$ vs $^{147}Sm/^{144}Nd$ ratios calculated in the mantle source at the different stages (1 to 4) compared to data measured in komatiites from the Komati Formation (this study, Blichert-Toft etal., 2015; Puchtel et al., 2013), Schapenburg (Puchtel et al., 2016) and Weltevreden (Puchtel et al., 2013). ICDP samples analyzed in this study for ^{146}Sm-^{142}Nd systematics are red circles with thick borders. The different stages are indicated by numbers in black circles: Stage 1: 4.567 Ga to 4.537 Ga - CHUR evolution; Stage 2: 4.537 Ga to 4027 Ga – Isotopic evolution of the solidified magma ocean; Stage 3: 4.027 Ga to 3.48 Ga - depletion in upper mantle; Stage 4: 3.48 Ga - komatiite formation. See Table 3 for details. The compositions residual liquids and cumulates formed during the crystallization of a magma ocean are also plotted in the figure. Lu/Hf and Sm/Nd are decoupled (upper left quadrant) when the bridgmanite proportion in a two-component mixture (bridgmanite/Ca-perovskite) exceeds 92% (proportions are indicated at the ends of the lines). Compositions are represented for 10, 20, 30, 40, 50 and 60% of crystallization (60% corresponds to the entire lower mantle). The OIB-MORB correlation illustrates the positive trend commonly observed in ocean-island and mid-ocean ridge basalts (mantle array from Chauvel et al., 2008).

Figure 9. Isotopic evolution of $\varepsilon^{143}Nd$, $\varepsilon^{176}Hf$, and $\mu^{142}Nd$ (right Y-axis) through time, from the start of solar system formation to the age of crystallization of Barberton komatiites. These 3 steps are described in detail in Table 3. Stars and circles represent the initial composition of ICDP drill core komatiites for $\varepsilon^{143}Nd$ and $\varepsilon^{176}Hf$, respectively (red symbols correspond to the initial defined from the isochrons). Measured $\mu^{142}Nd$ for the same samples are represented by the blue squares. Constants used in the calculation: $T_{1/2}$ ^{146}Sm=103 Ma (Friedman et al., 1966),

1001 $\lambda^{147}Sm = 6.54\times10^{-12}$ y^{-1}, $\lambda^{176}Lu = 1.865 \times10^{-11}$ y^{-1} (Scherer et al., 2001), CHUR
1002 parent/daughter ratios from Bouvier et al. (2008). The starting initial $^{142}Nd/^{144}Nd$ of
1003 the primitive mantle is considered equal to that of modern terrestrial samples (Bouvier
1004 and Boyet, 2016; Burkardt et al., 2016).
1005
1006 **Figure 10**. Results of Monte-Carlo simulations to test the sensitivity of the model
1007 (N=10 000). The range of input parameters tested at each of the four stages is
1008 indicated in the bottom left corner. Red circles and green squares are komatiite data
1009 from Barberton (same symbols as in Figure 8). ICDP samples analyzed in this study
1010 for ^{146}Sm-^{142}Nd systematics are red circles with thick borders. **A**) Present-day
1011 $^{176}Lu/^{177}Hf$ and $^{147}Sm/^{144}Nd$ modeled at each stage. CHUR compositions are from
1012 Bouvier et al. (2008). **B**) Histogram showing modeled Hf/Sm ratios at each stage.
1013 CHUR composition is similar to the primitive mantle composition defined by Palme
1014 and O'Neill (2014). Komatiite data were arbitrarily plotted at a data frequency of
1015 2000. c) Modeled Nd and Hf isotopic compositions at T_1 for Stage 1, T_2 for Stage 2,
1016 and T_3 for Stage 3. Epsilon values are calculated relative to the CHUR composition of
1017 Bouvier et al. (2008).
1018

Table

Table 1. Nd isotopic composition measured in komatiites and sediments drilled at BARB 1-5.
* $\mu^{142}Nd$ are calculated relative to the average $^{142}Nd/^{144}Nd$ ratio obtained for the JNdi-1 standards measured in the given TIMS session.

Sample	Depth, Type	Analytical Sequence	Method	$\mu^{142}Nd^{a}$	2SE ppm	$^{142}Nd/^{144}Nd$	2SE	$^{143}Nd/^{144}Nd$	2SE	$^{145}Nd/^{144}Nd$	2SE	$^{146}Nd/^{144}Nd$	2SE	$^{148}Nd/^{144}Nd$	2SE	$^{150}Nd/^{144}Nd$	2SE	$^{142}Ce/^{142}Nd$ x10^{6}	$^{144}Sm/^{144}Nd$ x10^{6}	Cycles
BARBERTON core komatiites																				
BARB1 GC/4	54.38m, Px spinifex	Seq.#1	Dyn_2L	0.5	3.4	1.141839	0.000004	0.512241	0.000002	0.348400	0.000001	0.722477	0.000030	0.241582	0.000001	0.236457	0.000002	14.0	55.4	540
BARB1 GC/4		Seq.#1, re-run	Dyn_2L	-5.5	4.1	1.141832	0.000005	0.512241	0.000002	0.348399	0.000001	0.723521	0.000046	0.241583	0.000001	0.236457	0.000002	2.2	70.2	540
BARB1 GC/4 weighted mean n=2				*-2.8*	*4.2*			*0.512241*	*0.000000*											
BARB1 GC/5	58.5m, Pyroxenite	Seq.#1	Dyn_2L	-4.3	5.1	1.141833	0.000006	0.512297	0.000002	0.348398		0.721149	0.000056	0.241580	0.000002	0.236450	0.000002	15.9	38.1	540
BARB1 GC/5		Seq.#1, re-run	Dyn_2L	-5.8	3.0	1.141832	0.000003	0.512296	0.000001	0.348400	0.000001	0.723095	0.000044	0.241582	0.000001	0.236454	0.000002	5.2	41.0	540
BARB1 GC/5		Seq.#, duplicate	Dyn_2L	0.3	3.7	1.141839	0.000004	0.512296	0.000002	0.348399	0.000001	0.724128	0.000007	0.241584	0.000001	0.236460	0.000002	4.6	46.8	473
BARB1 GC/5 weighted mean n=3				*-3.2*	*3.2*			*0.512296*	*0.000001*											
BARB1 GC/7	62.92m, Px spinifex	Seq.#1	Dyn_2L	-2.7	5.3	1.141835	0.000006	0.512209	0.000003	0.348399	0.000002	0.723173	0.000033	0.241581	0.000002	0.236456	0.000003	1.0	54.7	251
BARB1 GC/34A	85.72m, Hyaloclastite-block	Seq.#2	Dyn_2L	-3.7	3.7	1.141835	0.000004	0.512288	0.000002	0.348401	0.000001	0.723018	0.000020	0.241584	0.000001	0.236458	0.000002	81.5	7.4	540
BARB1 GC/34A		Seq.#2 re-load	Dyn_2L	-5.2	5.4	1.141833	0.000006	0.512289	0.000003	0.348401	0.000002	0.723755	0.000024	0.241583	0.000002	0.236460	0.000003	46.5	7.4	260
BARB1 GC/34A weighted mean n=2				*-4.6*	*1.1*			*0.512289*	*0.000000*											
BARB1 GC/9	89.23, Hyaloclastite	Seq.#2	Dyn_2L	-4.9	4.3	1.141833	0.000005	0.512230	0.000002	0.348399	0.000001	0.722228	0.000066	0.241584	0.000002	0.236456	0.000002	40.8	7.7	540
BARB1 GC/9		Seq.#2, re-run	Dyn_2L	-5.6	4.1	1.141832	0.000005	0.512229	0.000002	0.348400	0.000001	0.723563	0.000028	0.241583	0.000001	0.236458	0.000002	14.8	8.4	540
BARB1 GC/9 weighted mean n=2				*-5.3*	*0.5*			*0.512229*	*0.000001*											
BARB2 GC/1	252.60, Chill	Seq.#1	Dyn_2L	-5.9	4.4	1.141832	0.000005	0.512626	0.000002	0.348399	0.000001	0.722456	0.000089	0.241582	0.000002	0.236451	0.000002	9.8	16.6	540
BARB2 GC/1		Seq.#1 re-run	Dyn_2L	1.4	5.8	1.141840	0.000007	0.512626	0.000003	0.348400	0.000002	0.724164	0.000026	0.241582	0.000002	0.236456	0.000003	3.1	20.3	434
BARB2 GC/1 weighted mean n=2				*-1.8*	*5.2*			*0.512626*	*0.000000*											
BARB2 GC/6	257.66, Ol spinifex	Seq.#2	Dyn_2L	-9.7	3.4	1.141828	0.000004	0.512706	0.000002	0.348401	0.000001	0.722012	0.000061	0.241581	0.000001	0.236450	0.000002	4.7	4.6	540
BARB2 GC/6		Seq.#2, re-run	Dyn_2L	-5.8	3.4	1.141832	0.000004	0.512706	0.000002	0.348402	0.000001	0.722844	0.000041	0.241583	0.000001	0.236454	0.000002	2.6	5.7	540
BARB2 GC/6 weighted mean n=2				*-7.7*	*2.8*			*0.512706*	*0.000000*											
BARBERTON sedimentary rocks																				
B3-Ch3	Chert	Seq.#3	Dyn_4L	6.1	6.1	1.141842	0.000007	0.512241	0.000001	0.348404	0.000001	0.723301	0.000093	0.241582	0.000002	0.236455	0.000005	2.4	0.2	316
B3-Ch1	Chert	Seq.#3	Dyn_4L	-4.2	2.5	1.141831	0.000003	0.511443	0.000001	0.348403	0.000000	0.722536	0.000088	0.241580	0.000001	0.236462	0.000003	1.3	0.0	540
B3-Ch1	Chert	Seq.#3	Dyn_4L	-1.5	2.7	1.141834	0.000003	0.511443	0.000001	0.348403	0.000001	0.723524	0.000037	0.241583	0.000001	0.236461	0.000003	0.5	0.2	800
B3-Ch1 weighted mean n=2				*-2.8*	*3.9*															
B4-20	Si-rich sediments	Seq.#3	Dyn_4L	-0.4	2.2	1.141835	0.000003	0.511122	0.000001	0.348402	0.000001	0.721472	0.000047	0.241580	0.000001	0.236477	0.000003	1.0	0.2	540
B4-20	Si-rich sediments	Seq.#5, duplicate	Dyn_2L	0.9	3.2	1.141835	0.000004	0.511247	0.000001	0.348398	0.000001	0.722655	0.000016	0.241579	0.000001	0.236452	0.000002	18.3	0.0	540
B4-20	Si-rich sediments	Seq.#5, re-run	Dyn_2L	-4.8	5.4	1.141829	0.000006	0.511247	0.000002	0.348404	0.000002	0.723030	0.000017	0.241579	0.000002	0.236451	0.000003	43.3	0.0	540
B4-20	Si-rich sediments	Seq 7, duplicate	Dyn_2L	0.8	4.1	1.141838	0.000005	0.511106	0.000002	0.348392	0.000001	0.723094	0.000020	0.241579	0.000002	0.236457	0.000002	13.2	0.0	540
B4-20	Si-rich sediments	Seq 7, re-run	Dyn_2L	1.3	6.2	1.141839	0.000007	0.511106	0.000002	0.348391	0.000001	0.723996	0.000044	0.241581	0.000003	0.236462	0.000003	39.6	0.0	540
B4-20 weighted mean n=5				*-0.6*	*5.0*															
B4-31	Si-rich sediments	Seq 3	Dyn_4L	-8.8	6.8	1.141825	0.000008	0.511412	0.000002	0.348400	0.000001	0.722919	0.000088	0.241585	0.000002	0.236498	0.000007	1.5	0.3	540
B4-31	Si-rich sediments	Seq 4, duplicate	Dyn_4L	-10.5	4.9	1.141819	0.000006	0.511401	0.000001	0.348404	0.000001	0.721820	0.000093	0.241581	0.000002	0.236452	0.000005	3.8	0.1	400
B4-31	Si-rich sediments	Seq 4, re-run	Dyn_4L	-0.7	2.1	1.141830	0.000002	0.511418	0.000001	0.348403	0.000000	0.722389	0.000069	0.241579	0.000001	0.236447	0.000002	2.4	0.4	1080
B4-31	Si-rich sediments	Seq 5, duplicate	Dyn_2L	-9.9	5.0	1.141823	0.000006	0.511219	0.000002	0.348399	0.000001	0.721004	0.000059	0.241579	0.000001	0.236449	0.000001	10.3	0.0	540
B4-31	Si-rich sediments	Seq 5, re-run	Dyn_2L	-17.8	5.8	1.141814	0.000007	0.511216	0.000002	0.348401	0.000002	0.722958	0.000072	0.241580	0.000002	0.236446	0.000003	3.5	0.0	540
B4-31 weighted mean n=5				*-10.8*	*12.1*															
B4-48	Si-rich sediments	Seq 3	Dyn_4L	-2.1	5.8	1.141833	0.000007	0.511204	0.000002	0.348402	0.000001	0.722984	0.000160	0.241581	0.000002	0.236571	0.000005	2.9	2.4	320
B4-48	Si-rich sediments	Seq 7, duplicate	Dyn_2L	-14.5	5.6	1.141821	0.000006	0.510986	0.000002	0.348395	0.000001	0.723900	0.000060	0.241578	0.000002	0.236450	0.000003	15.2	0.0	540
B4-48 weighted mean n=2				*-8.2*	*17.4*															
B4-41	Si-rich sediments	Seq 5	Dyn_2L	-3.4	4.1	1.141830	0.000005	0.511608	0.000001	0.348402	0.000001	0.722564	0.000091	0.241579	0.000001	0.236452	0.000002	65.6	0.0	540
B4-41	Si-rich sediments	Seq 5, re-run	Dyn_2L	2.7	7.0	1.141837	0.000008	0.511608	0.000002	0.348396	0.000002	0.724886	0.000046	0.241578	0.000003	0.236455	0.000004	9.7	0.0	380
B4-41 weighted mean n=2				*0.4*	*8.6*															
B4-43	Si-rich sediments	Seq.#5	Dyn_2L	-1.7	3.8	1.141832	0.000004	0.511397	0.000001	0.348398	0.000001	0.722371	0.000031	0.241580	0.000002	0.236453	0.000002	9.3	0.0	540
B4-34	Si-rich sediments	Seq.#6	Dyn_2L	-7.4	3.7	1.141832	0.000004	0.511442	0.000001	0.348404	0.000001	0.722431	0.000022	0.241579	0.000001	0.236459	0.000002	6.3	0.0	540
B4-34		Seq.#7	Dyn_2L	-1.4	3.0	1.141836	0.000003	0.511438	0.000001	0.348395	0.000001	0.723726	0.000032	0.241576	0.000001	0.236457	0.000002	10.1	0.0	540
B4-34 weighted mean n=2				*-4.7*	*8.5*															
B5-355	Ca, Fe-rich sediments	Seq 3	Dyn_4L	-5.8	2.2	1.141829	0.000003	0.511331	0.000001	0.348403	0.000001	0.721478	0.000065	0.241580	0.000001	0.236456	0.000003	4.3	0.1	540
B5-355		Seq 3, re-run	Dyn_4L	-1.8	1.7	1.141833	0.000002	0.511331	0.000001	0.348403	0.000000	0.722893	0.000038	0.241580	0.000001	0.236457	0.000002	1.8	0.1	1200
B5-355 weighted mean n=2				*-4.0*	*5.6*															
B4-38	Ca, Fe-rich sediments	Seq 3	Dyn_4L	-1.5	2.8	1.141834	0.000003	0.511546	0.000001	0.348403	0.000001	0.722571	0.000092	0.241581	0.000001	0.236462	0.000003	1.9	0.3	540
B5-102	Ca, Fe-rich sediments	Seq 3	Dyn_4L	3.5	4.0	1.141839	0.000005	0.511122	0.000001	0.348405	0.000001	0.723042	0.000091	0.241581	0.000002	0.236462	0.000004	3.5	0.8	460
B4-40	Ca, Fe-rich sediments	Seq 3	Dyn_4L	-6.9	2.5	1.141827	0.000003	0.511427	0.000001	0.348403	0.000001	0.722354	0.000051	0.241581	0.000001	0.236454	0.000003	1.2	0.0	1080
B4-40	Ca, Fe-rich sediments	Seq 4, duplicate	Dyn_4L	-0.8	1.6	1.141830	0.000002	0.511433	0.000001	0.348404	0.000000	0.721638	0.000108	0.241579	0.000001	0.236436	0.000002	2.5	2.4	1080
B4-40	Ca, Fe-rich sediments	Seq 4, re-run	Dyn_4L	3.7	2.8	1.141835	0.000003	0.511420	0.000001	0.348405	0.000001	0.722263	0.000054	0.241580	0.000001	0.236442	0.000003	5.2	0.6	1080
B4-40 weighted mean n=3				*0.1*	*10.7*															
B5-108	Crustal-detritus rich sediments	Seq 4	Dyn_4L	0.1	1.8	1.141831	0.000002	0.510911	0.000001	0.348404	0.000000	0.722269	0.000039	0.241579	0.000001	0.236445	0.000002	9.1	0.1	1080
B5-108	Crustal-detritus rich sediments	Seq 7, duplicate	Dyn_2L	-6.4	9.1	1.141830	0.000010	0.511079	0.000004	0.348397	0.000006	0.724505	0.000090	0.241578	0.000004	0.236460	0.000005	16.6	0.0	460
B5-108	Crustal-detritus rich sediments	Seq 7, duplicate	Dyn_2L	-1.7	4.5	1.141835	0.000005	0.511080	0.000002	0.348397	0.000001	0.722926	0.000028	0.241579	0.000002	0.236460	0.000002	26.9	0.0	540
B5-108	Crustal-detritus rich sediments	Seq 7, re-run	Dyn_2L	-7.1	6.1	1.141829	0.000007	0.511079	0.000002	0.348390	0.000001	0.724320	0.000057	0.241578	0.000002	0.236450	0.000003	13.1	0.0	540
B5-108 weighted mean n=4				*-5.1*	*7.0*															
B4-16	Crustal-detritus rich sediments	Seq 5	Dyn_2L	-2.5	5.8	1.141831	0.000007	0.511198	0.000003	0.348398	0.000002	0.722981	0.000108	0.241579	0.000003	0.236450	0.000004	4.6	0.0	440
B4-16	Crustal-detritus rich sediments	Seq 6, duplicate	Dyn_2L	-3.1	3.8	1.141837	0.000004	0.511199	0.000001	0.348400	0.000001	0.722614	0.000024	0.241578	0.000001	0.236455	0.000002	4.0	0.0	540
B4-16	Crustal-detritus rich sediments	Seq 7, duplicate	Dyn_2L	-3.7	4.3	1.141833	0.000005	0.511195	0.000001	0.348396	0.000001	0.723322	0.000030	0.241578	0.000002	0.236457	0.000002	15.4	0.0	540
B4-16 weighted mean n=3				*-3.0*	*1.2*															
BS-730	Crustal-detritus rich sediments	Seq 3	Dyn_4L	2.0	2.3	1.141838	0.000003	0.511203	0.000001	0.348403	0.000000	0.722252	0.000086	0.241580	0.000001	0.236472	0.000002	0.0	0.1	540
JNdi-1 terrestrial standard																				
Average JNDI (n=7) sequence#1			Dyn_2L	0.0	3.5	1.141838	0.000004	0.512103	0.000001	0.348400	0.000002	0.722807	0.001461	0.241583	0.000001	0.236456	0.000001	0.3	0.5	540
Average JNDI (n=10) sequence#2			Dyn_2L	0.0	5.0	1.141839	0.000006	0.512104	0.000002	0.348400	0.000002	0.722366	0.001709	0.241583	0.000002	0.236456	0.000002	0.2	0.4	540
Average JNDI (n=7) sequence#3			Dyn_4L	0.0	4.2	1.141835	0.000005	0.512100	0.000003	0.348403	0.000001	0.720757	0.001110	0.241581	0.000002	0.236456	0.000006	1.2	0.0	540
Average JNDI (n=10) sequence#4			Dyn_4L	0.0	4.9	1.141831	0.000006	0.512099	0.000001	0.348403	0.000001	0.721672	0.001484	0.241581	0.000002	0.236451	0.000004	0.5	0.1	540
Average JNDI (n=4) sequence#5			Dyn_2L	0.0	4.1	1.141834	0.000005	0.512097	0.000002	0.348402	0.000002	0.721592	0.001381	0.241581	0.000002	0.236453	0.000004	0.6	0.0	540
Average JNDI (n=6) sequence#6			Dyn_2L	0.0	6.2	1.141841	0.000007	0.512102	0.000002	0.348401	0.000001	0.721671	0.000538	0.241578	0.000004	0.236452	0.000007	1.3	0.0	540
Average JNDI (n=6) sequence#7			Dyn_2L	0.0	4.3	1.141837	0.000005	0.512097	0.000002	0.348396	0.000001	0.719983	0.000008	0.241580	0.000002	0.236450	0.000004	0.3	0.0	540
BHVO-2 standard																				
BHVO2			Dyn_2L	-5.8	4.2			0.512974	0.000002	0.348400	0.000001	0.723430	0.000035	0.241582	0.000002	0.236456	0.000002	0.2	12.5	540
BHVO2		Seq 2re-run	Dyn_2L	1.6	4.2			0.512975	0.000002	0.348400	0.000001	0.722959	0.000009	0.241584	0.000002	0.236458	0.000002	0.2	12.1	540
BHVO2		duplicate	Dyn_2L	2.4	4.1			0.512977	0.000002	0.348401	0.000001	0.723109	0.000019	0.241582	0.000002	0.236453	0.000002	0.2	13.0	540
BHVO2		duplicate re-run	Dyn_2L	-3.4	4.3			0.512976	0.000002	0.348400	0.000001	0.724537	0.000045	0.241581	0.000001	0.236450	0.000002	0.1	15.9	540
BHVO2 mean n=4				*-1.4*	*3.9*															

	Primitive Mantle	Depleted MORB Mantle	Crust	Chert
$\mu^{142}Nd$	0	0	-8	0
$\varepsilon^{143}Nd_{,3.48Ga}$	0	2	-3.5	-1
$\varepsilon^{176}Hf_{,3.48Ga}$	0	4.5	-1.9	163
Sm	0.4347	0.27	1.6	0.763
Nd	1.341	0.713	5.9	2.593
Lu	0.07083	0.063	0.3	0.147
Hf	0.3014	0.199	1.4	0.024
Hf/Sm	0.693	0.74	0.88	0.03

Table 2.
Composition of the different end-members considered in the mixing model calculation. The composition of the Primitive Mantle is from Palme and O'Neill (2014). This mantle has chondritic ratios for refractory lithophile elements (Sm, Nd, Lu, Hf) and then has epsilon values at zero. The Depleted MORB Mantle composition is from Salters and Stracke (2004). Hf and Nd isotopic compositions have been calculated to account for an $\varepsilon^{143}Nd$ value of +2 at 3.48 Ga (mean value measured in Archean samples, see Boyet and Carlson 2005). The Hf isotopic composition is then estimated using the Hf-Nd mantle array of Chauvel et al. (2009). This equation defined from modern samples is also valid for Archean samples (Vervoort and Blichert-Toft, 1999). A mafic rock from the Ujaraaluk unit from the Nuvvuagittuq Greenstone Belt (sample PC-162 belonging to the enriched low-Ti group) is taken as an early crust analogue (O'Neil et al., 2011). Hf and Nd isotopic compositions were calculated considering the crust formed 4.3 Ga from a chondritic composition (O'Neil et al., 2008). Then the isotopic composition evolved until 3.45 Ga with parent/daughter ratios equal to those measured in the sample PC-162. Concentrations and parent/daughter ratios for chert correspond to the mean value of the 3 chert samples measured in Garçon et al. (2017). Hf-Nd isotopic compositions are calculated assuming an initial chondritic ratio and 0.8 Ga of evolution using the measured parent/daughter ratios. Cherts have extremely high Lu/Hf ratios and then develop with time highly radiogenic $^{176}Hf/^{177}Hf$ ratios. Archean sediments on the oceanic seafloor are assumed to have a residence time much higher than today (up to 200 Ma).

Table 3.

Stage 1 - 4.567 Ga to 4.537 Ga - CHUR evolution							
	Sm (ppm)	Nd (ppm)	Lu (ppm)	Hf (ppm)	$^{147}Sm/^{144}Nd$	$^{176}Lu/^{177}Hf$	Hf/Sm
Primitive mantle	0.435	1.341	0.07083	0.3014	0.1960	0.0335	0.69

Stage 2 - 4.537 Ga to 4027 Ga - Magma ocean crystallization in lower mantle conditions								
	D_{Sm}	D_{Nd}	D_{Lu}	D_{Hf}	Proportion %			
Bridgmanite	0.053	0.022	0.908	1.55	79			
Ca-Perovskite	13.98	11.18	9.14	1.42	5			
Ferropericlaose	0.049	0.036	0.110	0.076	16			
D	**0.75**	**0.58**	**1.17**	**1.30**				
fractional crystallization								
X = (1-F)	Sm (ppm)	Nd (ppm)	Lu (ppm)	Hf (ppm)	$^{147}Sm/^{144}Nd$	$^{176}Lu/^{177}Hf$	Hf/Sm	
0.3	0.339	0.830	0.081	0.372	0.2472	0.0310	1.10	cumulate
0.3	0.476	1.560	0.067	0.271	0.1843	0.0349	0.57	residual liquid

Stage 3 - 4.027 Ga to 3.48 Ga - Depletion in upper mantle condition (low pressure)								
	D_{Sm}	D_{Nd}	D_{Lu}	D_{Hf}	Proportion %	melt reaction %		
Olivine	0.0011	0.00042	0.02	0.011	53	-0.05		
Orthopyroxene	0.02	0.012	0.12	0.024	8	0.49		
Clinopyroxene	0.1509	0.0884	0.276	0.14	34	-1.31		
Garnet	0.23	0.064	7	0.4	5	-0.13		
D	0.06	0.03	0.46	0.08				
P	-0.218	-0.118	-1.214	-0.224				
batch melting non-modal								
F	Sm (ppm)	Nd (ppm)	Lu (ppm)	Hf (ppm)	$^{147}Sm/^{144}Nd$	$^{176}Lu/^{177}Hf$	Hf/Sm	
0.005	6.690	38.968	0.140	3.329	0.1038	0.0060	0.50	melt
0.005	0.444	1.372	0.066	0.256	0.1958	0.0368	0.58	residu

Stage 4 - 3.48 Ga - Melting event to produce the komatiite magma								
	D_{Sm}	D_{Nd}	D_{Lu}	D_{Hf}	%proportion			
Olivine	0.0011	0.00042	0.02	0.011	55			
Majorite	0.074	0.035	0.93	0.19	45			
D	**0.03**	**0.02**	**0.43**	**0.09**				
batch melting								
F	Sm (ppm)	Nd (ppm)	Lu (ppm)	Hf (ppm)	$^{147}Sm/^{144}Nd$	$^{176}Lu/^{177}Hf$	Hf/Sm	
0.3	1.372	4.409	0.110	0.703	0.1882	0.0223	0.51	liquid

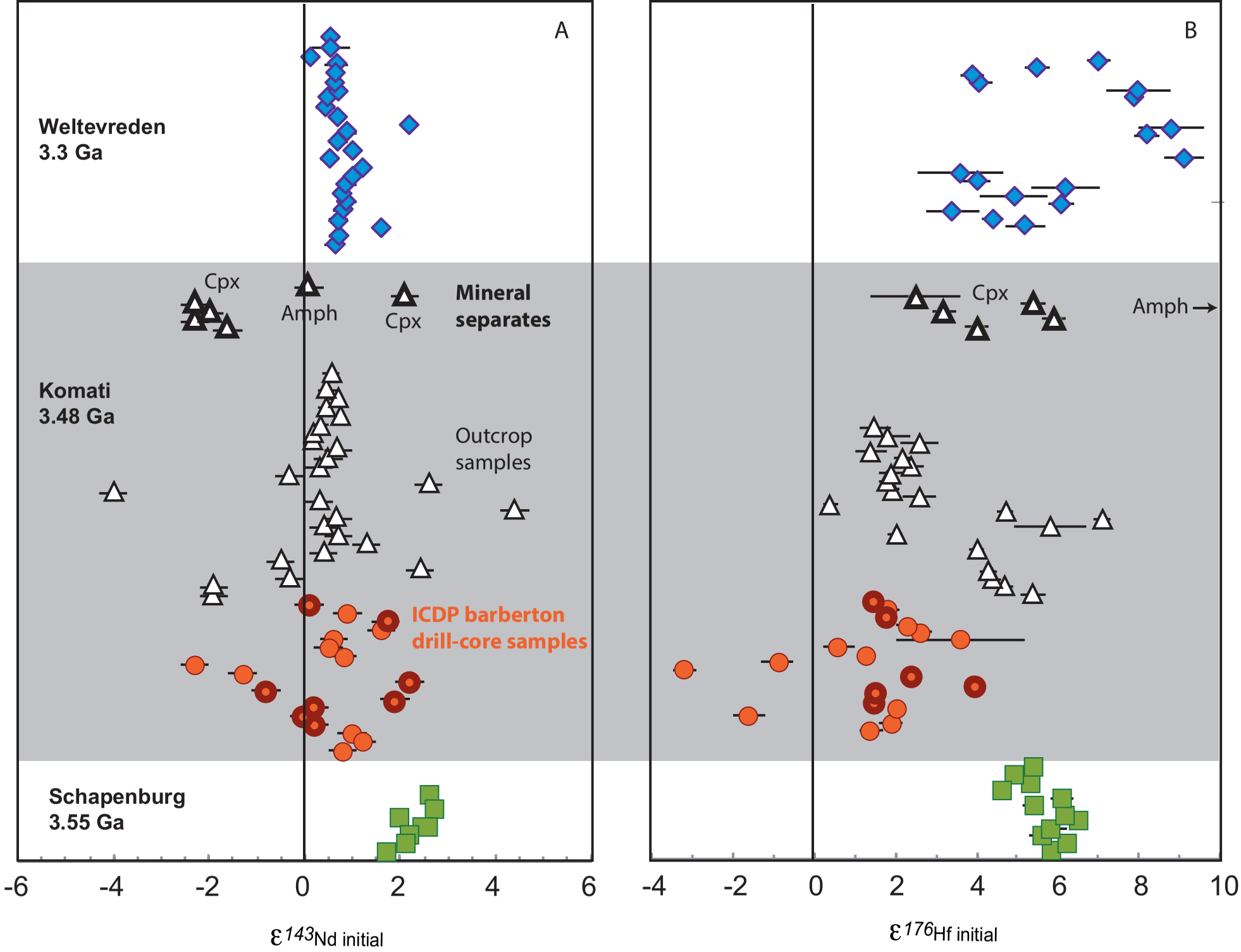

Figure 1 . Boyet et al.

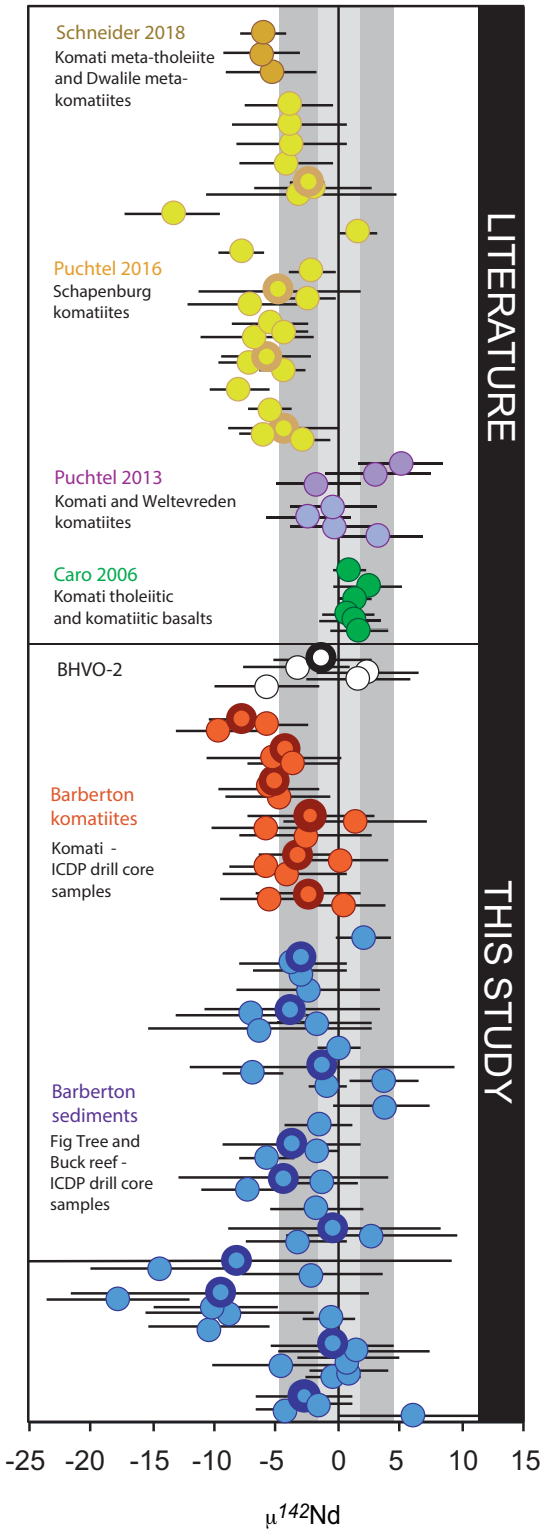

Figure 2. Boyet et al.

Figure 3

Click here to access/download;Figure;Figure 3.eps

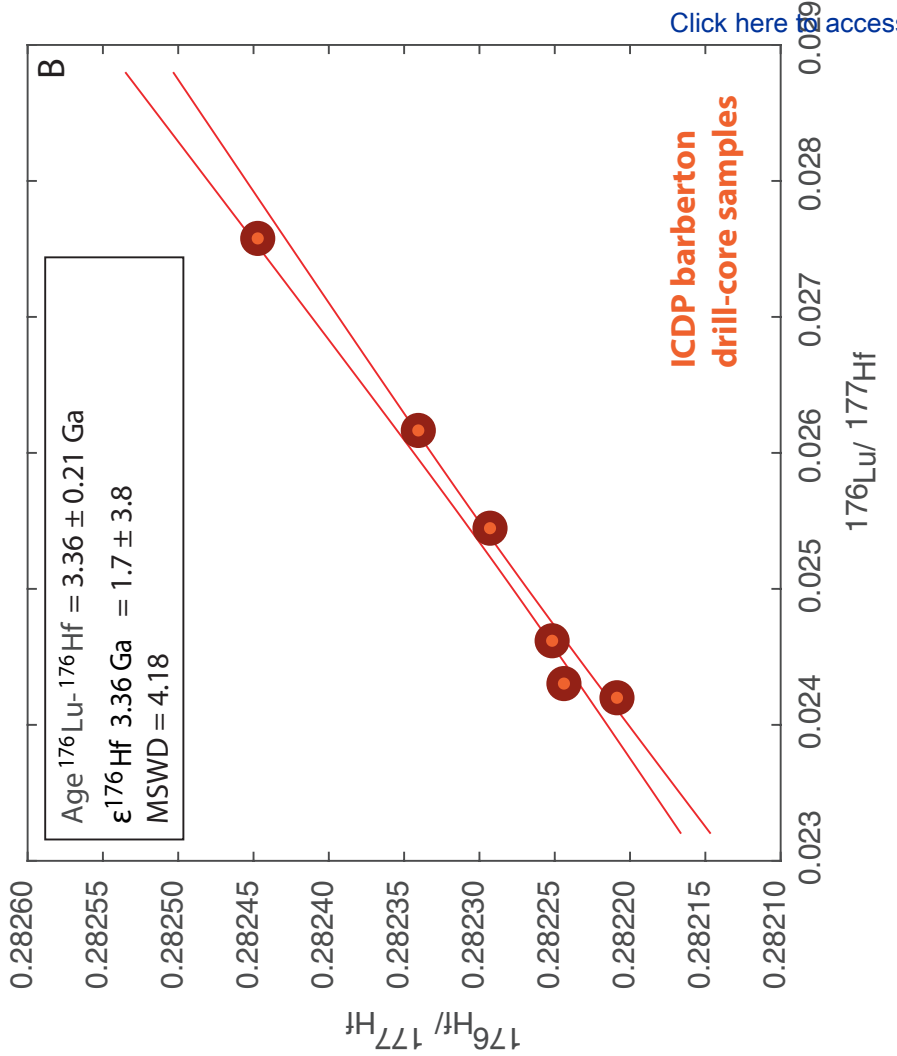

Figure 3. Boyet et al.

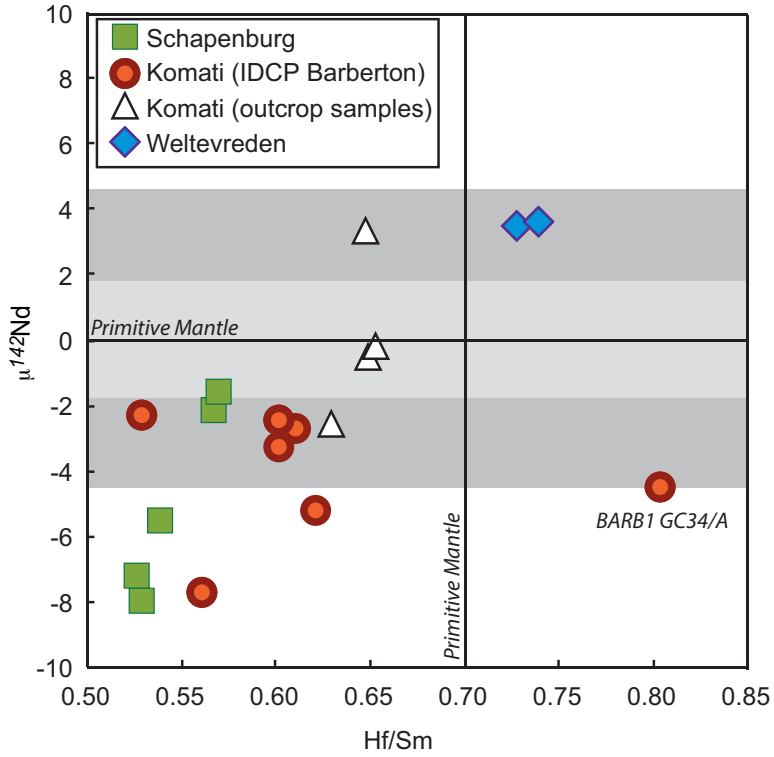

Figure 4. Boyet et al.

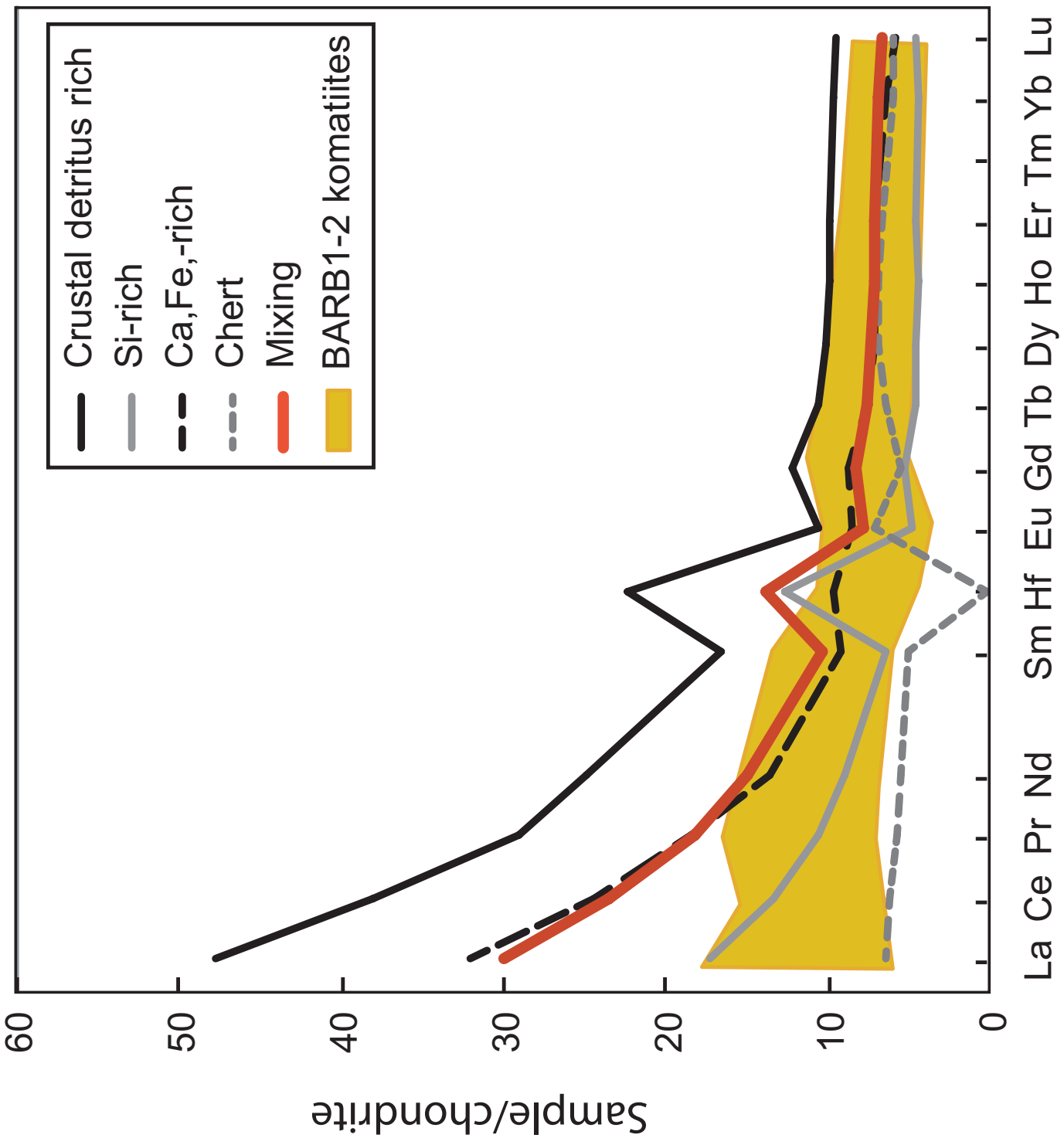

Figure 5. Boyet et al.

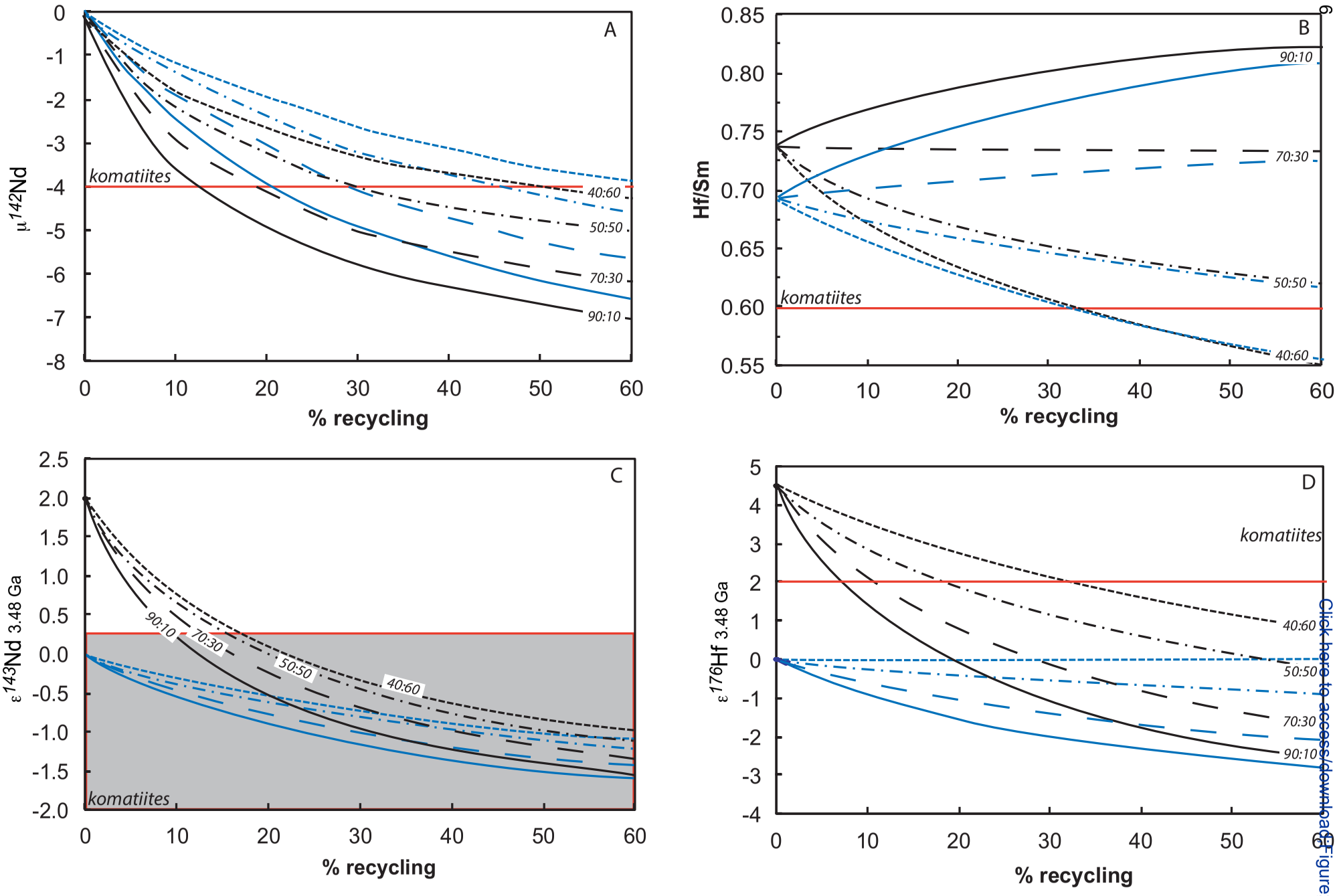

Figure 6. Boyet et al.

Figure 7

Click here to access/download;Figure;Figure 7.eps

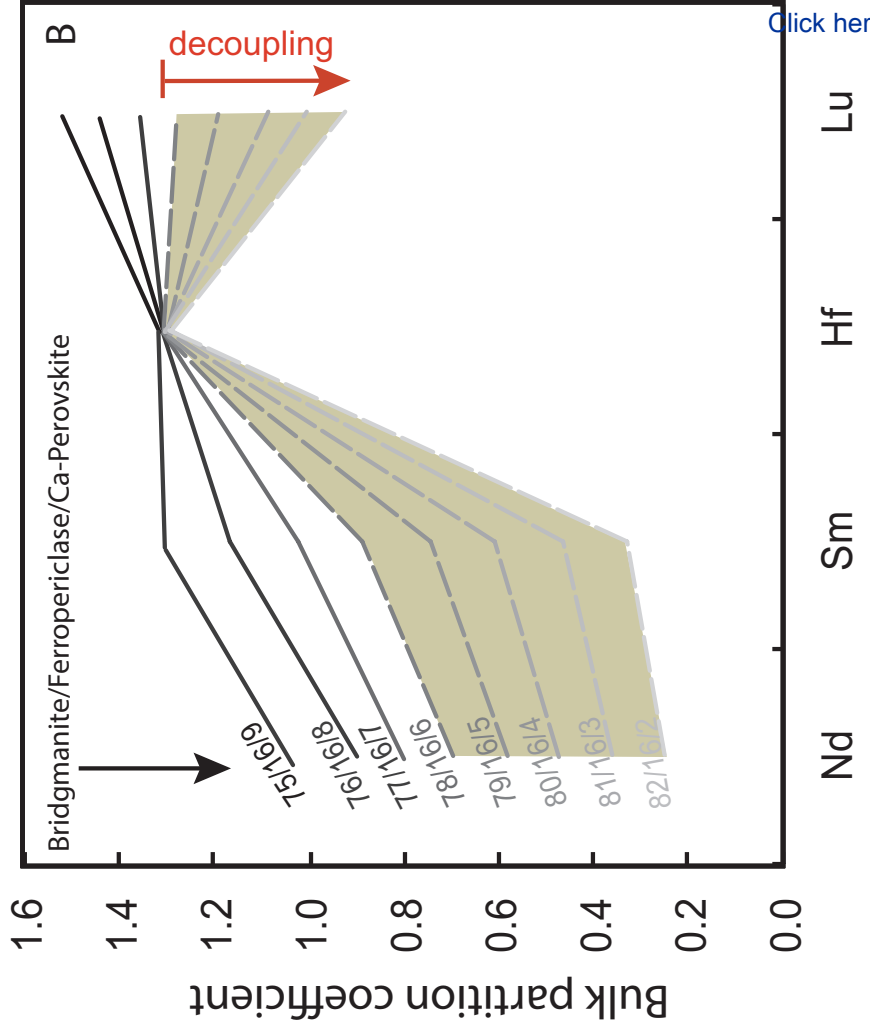

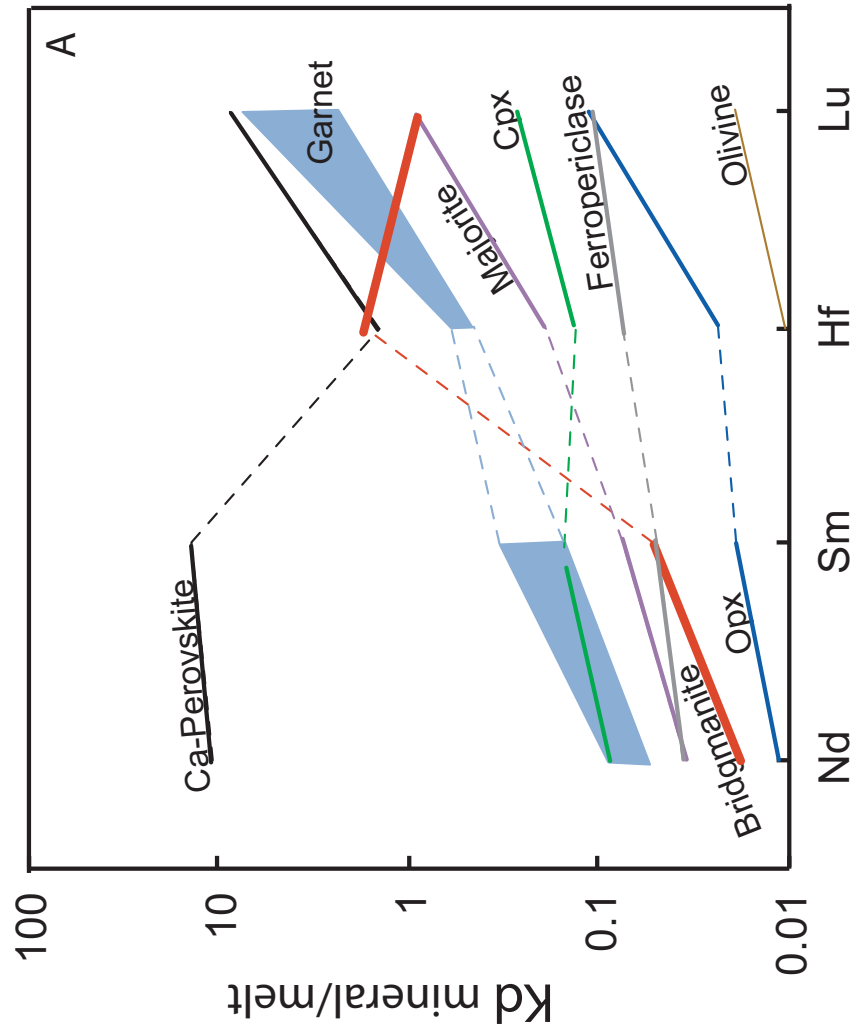

Figure 7. Boyet et al.

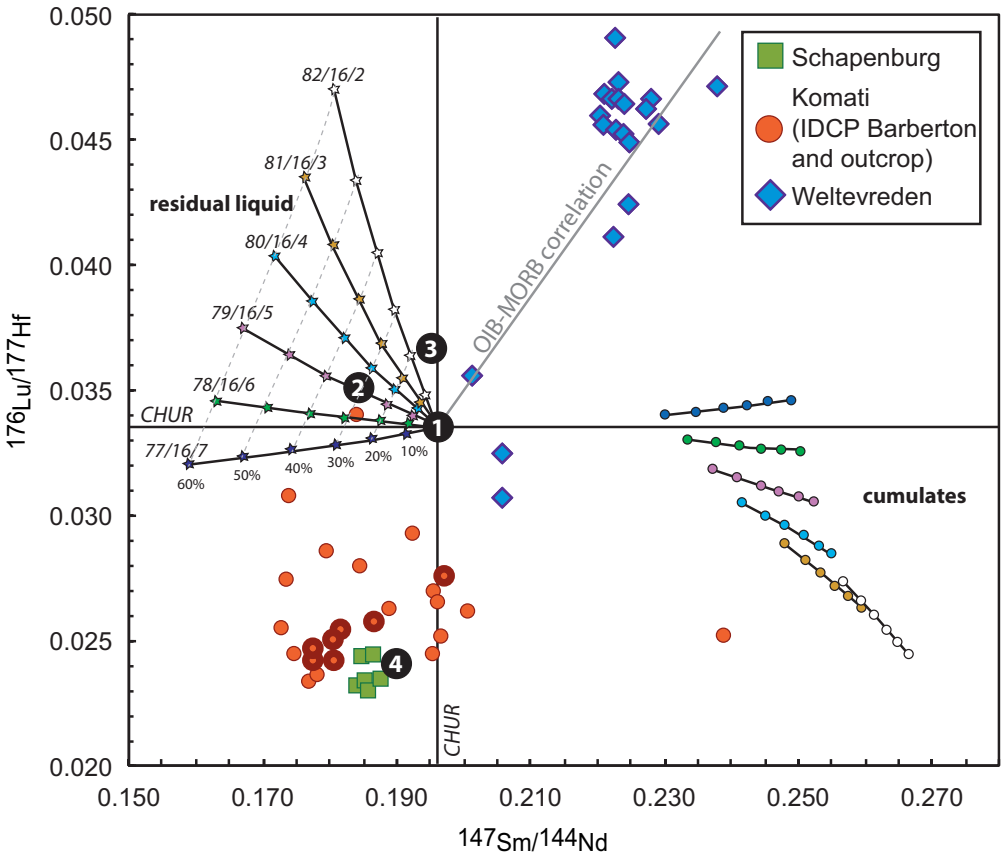

Figure 8. Boyet et al.

Figure 9

Click here to access/download;Figure;Figure 9.eps

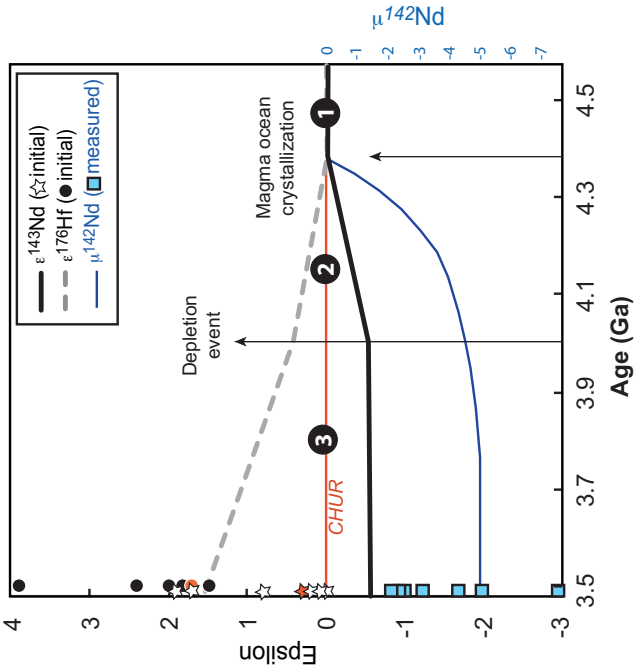

Figure 9. Boyet et al.